First results of SO_2 columns from FY-3F/OMS instrument observations

Huanhuan Yan[1,2,3], Andreas Richter[4], Xingying Zhang[1,2,3]*, Anja Schönhardt[4], Thomas Visarius[4], Qian Wang[1,2,3], Lu Zhang[1,2,3], Yichen Li[5], Chao Yu[5], Weihe Wang[1,2,3]

[1]National Satellite Meteorological Center (National Center for Space Weather), Beijing, 100081, China;
[2]Innovation Center for FengYun Meteorological Satellite (FYSIC), Beijing, 100081, China;
[3]Key Laboratory of Radiometric Calibration and Validation for Environmental Satellites/Key Laboratory of Space Weather, CMA, Beijing, 100081, China;
[4]Institute of Environmental Physics (IUP-UB), University of Bremen, Bremen, 28359, Germany;
[5]Aerospace Information Research Institute, Chinese Academy of Sciences, Beijing, 100094, China.

Correspondence to: Xingying Zhang (zxy@cma.gov.cn)

Abstract. Atmospheric SO_2 has a significant impact on the urban environment and on global climate. Remote sensing provides an unprecedented tool for the continuous and real-time monitoring of atmospheric SO_2 from volcanic eruptions and anthropogenic emissions. The Ozone Monitoring Suite (OMS) onboard the Chinese FENGYUN-3F (FY-3F) satellite launched in August 2023 is a new hyperspectral UV-VIS instrument in the FY-3 family of satellites, aiming to obtain information about atmospheric trace gases. In this study, we use the OMS Nadir (OMS-N) top-of-atmosphere (TOA) measurements and Differential Optical Absorption Spectroscopy (DOAS) inversion to for the first time retrieve global SO_2 columns from these measurements. Based on the characteristics of the OMS instrument and the performance of its L1 data, specific schemes including solar spectrum selection, spectral soft calibration, and background offset correction were developed to effectively reduce along-track stripes and across-track asymmetry found in the raw OMS SO_2 retrievals. The accuracy of FY-3F/OMS SO_2 retrievals was evaluated by comparing them with the DOAS and COvariance-Based Retrieval Algorithm (COBRA) SO_2 products from the TROPOspheric Monitoring Instrument (TROPOMI) onboard Copernicus Sentinel-5 Precursor (Sentinel-5P) over three typical areas: clean oceanic regions, volcanic eruption regions, and anthropogenic emission regions. The results indicate that the OMS SO_2 retrievals exhibit good stability over clean oceanic regions (with a precision of approximately 0.15 DU), successfully capture volcanic SO_2 plumes, and effectively detect the elevated SO_2 columns from anthropogenic emissions in regions such as the Middle East, Eastern India, and Northern Russia. Detector non-uniformity and Air mass factor (AMF) uncertainty remains the primary error source of this first version of OMS SO_2 retrievals. This study is the first to present SO_2 retrievals from FY-3F/OMS observations, which is crucial for a comprehensive understanding of OMS's capability in SO_2 retrievals.

Deleted: FY3F/OMS

Deleted: Huanhuan Yan[1], Andreas Richter[2], Xingying Zhang[1]*, Anja Schönhardt[2], Thomas Visarius[2]
[1]Key Laboratory of Radiometric Calibration and Validation for Environmental Satellites, National Satellite Meteorological Center (National Center for Space Weather), Innovation Center for FengYun Meteorological Satellite, Beijing, 100081, China.
[2]Institute of Environmental Physics (IUP-UB), University of Bremen, Bremen, 28359, Germany.

Deleted: initial

Deleted: FY3F/OMS

1 Introduction

Sulfur dioxide (SO_2) is a short-lived trace gas in the atmosphere that affects regional air quality and global climate change. SO_2 is primarily released by anthropogenic activities (e.g., smelting of sulfur ore, combustion of coal, the oil and gas industry, emissions of motor vehicles) and natural phenomena (e.g., volcanic and biological processes) (Finlayson-Pitts and Pitts Jr, 1999; Cullis and Hirschler, 1980; Seinfeld and Pandis, 2016). SO_2 injection from a volcanic eruption can reach up to the upper troposphere/lower stratosphere, not only affecting global climate but also posing a threat to aviation, along with volcanic ash. Through reaction with hydroxyl radicals (OH) and water, atmospheric SO_2 can be rapidly converted into sulfate aerosols. These aerosols both scatter and absorb solar and terrestrial radiation, affecting the radiation balance of the atmosphere (cooling or warming effect) (Twomey, 1977). Sulfate particles formed from anthropogenic SO_2 emissions not only influence atmospheric visibility in the boundary layer but also contribute to acid rain which in turn damages ecosystems. Low-Earth-orbit (LEO) satellite remote sensing offers the advantages of near global coverage, short-term periodic observation capabilities, and continuous spatial coverage. Due to the strong absorption characteristics of SO_2 in the ultraviolet (UV) spectrum, especially in the 300–400 nm wavelength range, atmospheric SO_2 information can be obtained from the reflected TOA radiance spectrum. Since the first UV-based satellite observation of large amounts of SO_2 from the El Chichón volcanic eruption in 1982 by TOMS (Krueger, 1983), hyperspectral UV satellite instruments have been used to quantitatively monitor the spatial and temporal distribution of SO_2 and its dispersion following volcanic eruptions. This compensates for the limitations of ground-based measurements, such as the high cost of dense in-situ observation networks and instrument maintenance (Krueger, 1983; Carn et al., 2005; Carn et al., 2007; Carn et al., 2009).

With the launch of a series of hyperspectral UV detection instruments, including the Global Ozone Monitoring Experiment (GOME) (Burrows et al., 1999; Khokhar et al., 2005; Eisinger and Burrows, 1998), the Scanning Imaging Absorption Spectrometer for Atmospheric Cartography (SCIAMACHY) (Gottwald and Bovensmann, 2010; Richter et al., 2006), the Ozone Monitoring Instrument (OMI) (Levelt et al., 2006), the Global Ozone Monitoring Experiment-2 (GOME-2) (Heue et al., 2010; Munro et al., 2006; Richter, 2009), the Ozone Mapping and Profiler Suite (OMPS) (Yang et al., 2013; Flynn et al., 2006), TROPOMI (Theys et al., 2019; Voors et al., 2017; Veefkind et al., 2012), and the Environmental Trace Gas Monitoring Instrument (EMI) (Chen et al., 2021; Zhao et al., 2020; Yan et al., 2021), satellite detection has been widely applied to monitor global SO_2 variations and to support research on climate change, atmospheric chemistry, and the atmospheric environment.

FY-3F/OMS is a newly launched Chinese UV-VIS hyperspectral sensor that provides global observations with 7 km × 7 km spatial resolution at nadir and a morning overpass time. For a thorough understanding of the OMS SO_2 product, this study presents OMS SO_2 retrievals by using the OMS measurements and DOAS inversion, and compares them with TROPOMI DOAS and TROPOMI COBRA SO_2 products over clean oceanic regions, volcanic eruption regions, and anthropogenic emission regions. This paper is organized as follows. Section 2 gives a brief introduction to the FY-3F/OMS instrument. Section 3 describes the detailed procedures used to retrieve the SO_2 columns from FY-3F/OMS observations, including solar

Deleted: hydroxide

Deleted: S

Deleted: concentrations and diffusion trends before and after

Deleted: FY3F/OMS

Deleted: FY3F/OMS

Deleted: FY3F/OMS

spectrum selection, spectral soft calibration, SO_2 slant column density (SCD) retrieval, background offset correction, and the approach for AMF calculation used. Section 4 provides the OMS SO_2 column results, followed by comparisons with the TROPOMI DOAS and TROPOMI COBRA SO_2 products. Section 5 discusses error sources of OMS SO_2 retrievals, including the instrument-related errors and DOAS SCD spectral fitting errors in OMS SO_2 SCD retrievals, errors introduced by the AMF approach taken, and the residual errors after background offset correction. The last section summarizes the main results and offers conclusions, along with suggestions for future improvements.

Deleted: simplified

Deleted: simplified

2 The FY-3F/OMS Instrument

Deleted: FY3F/OMS

Table 1. The main characteristics of the FY-3F/OMS-N instrument

Parameter	Nadir column measurement	Nadir profile measurement
Spectral range	VIS: 307~493nm	UV1:250~300nm UV2: 300~320nm
Spectral resolution	0.5~0.6nm	UV1: ~1.0nm UV2: ~0.5nm
Spectral accuracy	0.01nm	0.05nm
Spatial resolution at nadir point	7 km x 7 km	UV1: 21 km x 28 km UV2: 7 km x 7 km
Atmospheric products	O_3, NO_2, SO_2, HCHO, AOD, cloud fraction and pressure	O_3 profile
Field of view	112°	
Orbit observation	polar sun synchronous morning orbit	
Orbit altitude	836 km	
Equator crossing time	10:00 AM (local time)	
Duty Cycle	Daytime only	
Revisit Time:	24 hours	

The FY-3F satellite, the 21st in China's FengYun series, was successfully launched on August 3, 2023. It operates in a sun-synchronous orbit at an altitude of 836 km, with a descending node equatorial overpass time of 10:00 AM. Equipped with 10 advanced atmospheric instruments, FY-3F is designed to provide high-quality data for weather forecasting, climate monitoring, and environmental research, contributing significantly to global meteorological and environmental observations. The Ozone Monitoring Suite (OMS) onboard FY-3F satellite is a new instrument in the FY-3 family of satellites. It has two observation modes: Nadir (OMS-N) and Limb (OMS-L) (Wang et al., 2024). While OMS-L provides information on the vertical distribution of O_3, OMS-N is mainly used to obtain column information on trace gases such as O_3, NO_2, SO_2, and

HCHO, and aerosols, as well as vertical profiles of O_3. OMS-N operates using a push-broom observation technique to obtain daily global measurements, with a wide Field of View (FOV) of 112°. It incorporates two imaging grating spectrometers covering the UV (250-320 nm) and VIS (307-493 nm) bands, where the UV measurements are divided into the UV1 (250-300 nm) and UV2 (300-320 nm) sub-bands. Each spectrometer uses a 1024 × 1024 pixel imaging array, with one dimension recording spatial information along the slit and the other recording spectral information. To enhance the signal-to-noise ratio (SNR) of the original detector rows, OMS L1 applied an onboard spatial binning strategy: sets of 16 pixels were averaged to yield 58 cross-track spatial rows in the UV1 band, and 4 pixels were averaged to produce 238 cross-track spatial rows in the UV2 and VIS bands, respectively (Wang et al., 2024). The remaining spatial rows were reserved for calibration purposes. The OMS-N VIS band (307-493 nm) was used for the retrieval of OMS SO_2 columns in this study. It has a high spatial resolution of 7 km x 7 km at the nadir point, with a spectral resolution of 0.5-0.6 nm (Table 1). FY-3F/OMS data can be downloaded from the website http://data.nsmc.org.cn/DataPortal/en/home/index.html.

3 SO_2 column retrievals from FY-3F/OMS

The SO_2 retrieval from FY-3F/OMS involves radiance normalization, spectral soft calibration, convolution of SO_2 and O_3 cross-sections and Ring spectrum with the OMS-N Instrument Spectral Response Function (ISRF), DOAS fitting to obtain SO_2 SCD, AMF conversion to vertical column density (VCD), and background offset correction to reduce striping and across-track asymmetries. It should be noted that, due to the current unavailability of synchronized and reliable OMS cloud and aerosol products, the effects of clouds and aerosol on SO_2 retrievals were not considered in this study. For the OMS SO_2 product, it is recommended to use retrieval results with a solar zenith angle smaller than 70°, near-nadir and cloud-free pixels.

3.1 Solar irradiance

Using the satellite measured solar irradiance for the DOAS SO_2 retrieval can effectively reduce instrument-related errors. However, due to the degradation and non-uniformity of the diffuser plate of OMS, the OMS L1 irradiance measurements experienced increasing errors after launch, especially in the shortwave UV region. For example, after one year on orbit, the intensity of OMS irradiance at the shorter wavelength of 317 nm has decreased by about 8.83%, while at the longer wavelength of 331 nm, it has decreased by about 6.07%. Therefore, in this study the Total and Spectral Solar Irradiance Sensor-1 (TSIS-1) Hybrid Solar Reference Spectrum (HSRS) hybrid solar reference spectrum (Coddington et al., 2021) was used for OMS SO_2 retrievals instead of OMS daily measured solar irradiance. The TSIS-1 HSRS hybrid solar reference spectrum was developed by normalizing high spectral resolution solar datasets to the absolute irradiance scale of the TSIS-1 Spectral Irradiance Monitor (SIM) and the CubeSat Compact SIM (CSIM). The high spectral resolution solar data are sourced from the Air Force Geophysical Laboratory (AFGL) ultraviolet solar irradiance balloon observations, the ground-based Quality Assurance of Spectral Ultraviolet Measurements in Europe Fourier Transform Spectrometer (QASUMEFTS) solar irradiance observations, the Kitt Peak National Observatory (KPNO) solar transmittance atlas, and the semi-empirical

Deleted: OMS-N operates using a push-broom observation technique to obtain daily global measurements, with a wide Field of View (FOV) of 112° , covering three spectral bands: UV1 (250-300 nm), UV2 (300-320 nm), and VIS (307-493 nm). To enhance the signal-to-noise ratio (SNR) of the original detector rows, sets of 16 pixels are averaged to yield 58 spatial rows in the UV1 band, and four pixels are averaged to acquire 238 spatial rows in the UV2 and VIS bands, respectively (Wang et al., 2024). …

Deleted: FY3F/OMS

Deleted: FY3F/OMS

Deleted: The SO_2 retrieval from FY3F/OMS mainly involves the following steps. (1) Firstly, the OMS-N L1 earth radiance is normalized to the Earth-Sun distance of 1AU, while the solar irradiance is obtained by convolving the Total and Spectral Solar Irradiance Sensor (TSIS) Hybrid Solar Reference Spectrum (HSRS) (Coddington et al., 2021) (See section 3.1 for more information) with the Instrument Spectral Response Function (ISRF) of OMS-N. (2) Secondly, the 312-326 nm region is chosen as the retrieval fitting window of the OMS SO_2 column. (3) Thirdly, spectral soft calibration is performed using the absorption peaks and valleys of the solar reference spectrum. (4) Fourthly, the cross sections of SO_2 and O_3 in 312-326 nm are convolved with the ISRF. (5) Fifthly, the Ring spectrum is calculated using the SCIATRAN Radiative Transfer Model (Rozanov et al., 2005). (6) Sixthly, SO_2, O_3 and Ring cross-sections together with a third-order polynomial are used in the DOAS fitting process to obtain the SCD of OMS SO_2. (7) Seventhly, the AMF is applied to get vertical column density (VCD). (8) Finally, a specific correction scheme for OMS background offset is applied to effectively reduce along-track stripes and across-track asymmetries in the initial OMS SO_2 retrievals. …

Deleted: (for more information see section 5.1).

Deleted: TSIS HSRS

Solar Pseudo Transmittance Spectrum (SPTS) atlas. The TSIS-1 HSRS spans 202–2730 nm at 0.01 to ~0.001 nm spectral resolution with uncertainties of 0.3% between 460 and 2365 nm and 1.3% at wavelengths outside that range (Coddington et al., 2021). The TSIS-1 HSRS hybrid solar reference spectrum was convolved with the OMS-N ISRF to match the spectral characteristics of OMS radiance.

3.2 Spectral soft calibration

Before the DOAS fitting retrieval, spectral soft calibration was applied to the FY-3F/OMS radiance data. This procedure corrects wavelength shifts caused by instrument drift, temperature fluctuations, radiation effects, and nonlinearities, by using known absorption features. It ensures the spectral accuracy and consistency of the OMS radiances, which is essential for accurate SO_2 retrieval and for reducing the impact of calibration-related errors.

The spectral soft calibration is performed using the peaks and valleys of the TSIS-1 HSRS hybrid solar reference spectrum (Van Geffen and Van Oss, 2003; Coddington et al., 2021). The detailed process includes: 1) Selecting the high-resolution hybrid solar reference spectrum (Coddington et al., 2021), and convolving the reference spectrum with the slit function of the FY-3F/OMS instrument; 2) Fitting the ratio of the solar reference spectrum to the observed radiance spectrum with a low-order polynomial to enhance the observed radiance spectrum; 3) For each observed radiance spectrum in the SO_2 fitting window, Gaussian peak-finding is performed to match the peak position of a set of Fraunhofer lines with their corresponding wavelengths. A least-squares method is used to fit the spectral line wavelengths and the peak position number data with a third-order polynomial, generating a spectral calibration equation for each observed pixel. Then the spectral soft calibration of the FY-3F/OMS radiance is realized by using the above spectral calibration equation.

3.3 DOAS SCD retrieval

3.3.1 SO_2 fitting window

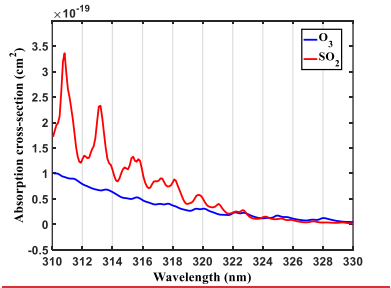

Figure 1: Absorption cross sections of SO_2 and O_3 in the wavelength range 310-330 nm (Bogumil et al., 2003).

Deleted: The FY3F/OMS-N ISRF was determined using tunable laser scanning with a step size of 0.02 nm, providing the relative response of each detector pixel on the focal plane arrays to monochromatic illumination (Wang et al., 2024). It varies in both the spectral and spatial dimensions of the two large array detectors. The shape of the FY3F/OMS-N ISRF exhibits a flat top in the central peaks because OMS-N adopts a stereoscopic slit observation mode (Wang et al., 2024). The TSIS HSRS hybrid solar reference spectrum provides high accuracy solar irradiances, but as it was not measured with the OMS-N instrument, any calibration issues in the radiances do not cancel in the DOAS retrieval. Therefore, its use may lead to systematic overestimation or underestimation in the retrieved SO_2 columns, as well as along-track stripes, which cannot be fully corrected through post-processing algorithms.

Deleted: FY3F/OMS

Deleted: Spectral soft calibration can

Deleted: factors such as

Deleted: effects

Deleted: ,

Deleted: to adjust the initial L1 data

Deleted: The spectral soft calibration process

Deleted: minimizing

Deleted: on the SO_2 retrieval

Deleted: FY3F/OMS

Deleted: FY3F/OMS

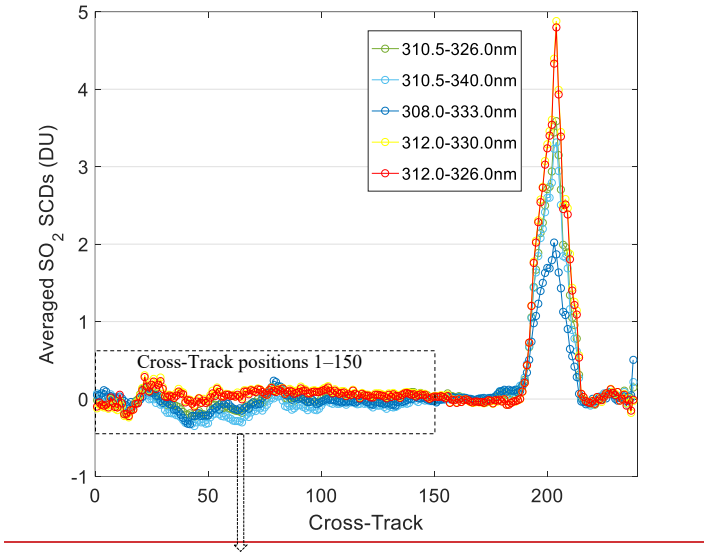

Fitting window (nm)	Standard deviation (DU)	Mean value (DU)
312–326	0.08	0.04
310.5–326	0.09	-0.03
310.5–340	0.1	-0.1
308–333	0.09	-0.04
312–330	0.09	0.06

Figure 2: Row-averaged SO_2 retrievals from OMS rows 700 to 870 of orbit 20240823_1036 by using different spectral fitting windows.

The selection of the retrieval fitting window is crucial for the accuracy of OMS SO_2 retrievals, which significantly affect OMS capability in monitoring SO_2 from volcanic and anthropogenic sources. A suitable fitting window helps to reduce the impact of interfering gases (O_3), to enhance the SO_2 information content in the satellite signal and to obtain reliable SO_2 results. In this study, the 312–326 nm fitting window was selected for the OMS SO_2 retrievals based on the following considerations.

(1) Shorter wavelengths, despite stronger SO_2 absorption (Fig. 1), suffer from lower SNR and TOA radiance saturation over volcanic plumes, while longer wavelengths introduce more noise due to weaker absorption and O_3 interference, especially under low anthropogenic emissions.

(2) The selected fitting window (312–326 nm) is consistent with the widely used TROPOMI SO_2 product (Theys et al., 2017), facilitating intercomparison and validation of the OMS SO_2 retrievals. For the first results of OMS SO_2 results in this study, we did not adopt multiple fitting windows for different SO_2 concentration conditions as implemented in the TROPOMI product.

(3) Comparisons of SO_2 retrievals from different fitting windows commonly used in published studies—312–326 nm (Theys et al., 2017), 310.5–326 nm (Theys et al., 2021), 310.5–340 nm (Li et al., 2013), 308–333 nm (Yang et al., 2009, 2013), and 312–330 nm (Nowlan et al., 2011)—over the Sundhnúkur volcano and the surrounding clean region on 23 August 2024 (Fig.) show that the 312–326 nm window has higher SO_2 values within the volcanic plume and lower standard deviations and mean values in the clean region (cross-track positions 1–150). These results demonstrate the suitability of the 312–326 nm fitting window for OMS SO_2 retrievals. The discrete wavelengths (310.8, 311.9, 313.2, and 314.4 nm) used in the Band Residual Difference (BRD) algorithm (Krotkov et al., 2006) were not considered in this study because the OMS SO_2 retrieval is based on DOAS algorithm that employs a hyperspectral UV fitting window. The 300–335 nm fitting window employed in the EISF algorithm (Yang et al., 2010) was also not considered in this study because the OMS VIS band starts at 307 nm, and the OMS UV2 spectral range (300–320 nm) requires further calibration.

3.3.2 Ring effect

The Ring effect is an important factor influencing the accuracy of SO_2 retrieval results due to the pronounced filling-in features of the Ring spectrum in the UV region (Fig. 3). It redistributes photon energy and leads to the filling-in of Fraunhofer and atmospheric absorption lines (Sioris and Evans, 1999; Fish and Jones, 1995; Chance and Spurr, 1997; Vountas et al., 1998). For OMS SO_2 column retrievals using the DOAS method, the Ring effect is considered as a pseudo-absorption effect, and the Ring spectrum calculated using the SCIATRAN radiative transfer model (Rozanov et al., 2005) is included as a pseudo-absorber in the spectral fitting process, as shown in Equation (1).

$$-\ln\frac{\pi * I(\lambda)}{F(\lambda) * \cos(SZA)} = \sigma_{SO_2}(\lambda) \times SCD_{SO_2} + \sigma_{O_3}(\lambda) \times SCD_{O_3} + \sigma_{Ring}(\lambda) \times C_{Ring} + P(\lambda) + E(\lambda) \quad \text{(Eq. 1)}$$

Where $I(\lambda)$ and $F(\lambda)$ are the satellite-observed radiance and the solar reference spectrum convolved with the OMS ISRF, SZA is the Solar Zenith Angle, $\sigma_{SO_2}(\lambda)$ and $\sigma_{O_3}(\lambda)$ are the absorption cross-section of SO_2 and O_3, SCD_{SO_2} and SCD_{O_3} are the slant column density of SO_2 and O_3, $\sigma_{Ring}(\lambda)$ is the Ring spectrum calculated using the SCIATRAN model and convolved with the OMS ISRF, C_{Ring} is the Ring absorption coefficient determined by the fitting, $P(\lambda)$ is a low-order polynomial, and $E(\lambda)$ is the error term.

Note that in this study a fixed Ring spectrum calculated using the SCIATRAN model under typical atmospheric and surface conditions and observational geometry (SZA=30°, Viewing Zenith Angle (VZA)=0°, Relative Azimuth Angle (RAA)=0°,

surface reflectance (AS)=0.05, surface height above sea level (HS) (also referred to as terrain height)=0 km, ozone column=275 DU, clear sky) is used in the DOAS fitting for all OMS measurements. Variations of the Ring spectrum due to different atmospheric conditions and viewing geometries are not considered, since applying the Ring lookup table would be computationally costly and its impact on OMS SO_2 SCD retrievals is limited. A detailed error analysis of this fixed Ring approach is discussed in Section 5.1.3.

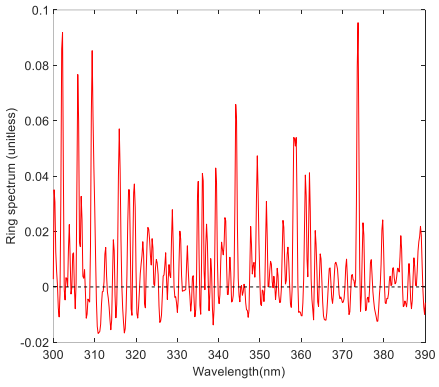

Figure 3: Ring spectrum calculated with the SCIATRAN model, convolved with the OMS nadir ISRF. SCIATRAN forward settings are SZA=30°, VZA=0°, RAA=0°, Surface albedo=0.05, Ozone column=275 DU, Clear sky.

3.3.3 Spectral fitting

The retrieval of the FY-3F/OMS SO_2 SCD is primarily based on the classical DOAS theory (Platt and Stutz, 2008). It utilizes Beer-Lambert's law and the satellite hyperspectral radiance observations in the UV fitting window to derive the SO_2 SCD along the entire photon path. First, the absorption cross-section of SO_2 and O_3, measured under specific laboratory conditions with a higher spectral resolution and different sampling points than those of OMS observations, are convolved with the OMS ISRF to match the spectral resolution of the OMS instrument. Secondly, atmospheric extinction is divided into two components: a fast-varying part with wavelength, typically associated with narrow absorption features of SO_2 and O_3, and a slow-varying part with wavelength, related to broad spectral features of absorption and atmospheric scattering processes such as Rayleigh and Mie scattering. A low-order polynomial is used to remove the slow-varying components, while preserving the fast-varying part related to SO_2 and O_3 absorption. Finally, the slow-varying part of satellite-observed TOA reflectance (the ratio of L1 radiance to irradiance data) are removed by subtracting a low-order polynomial, and the atmospheric SO_2 SCD is obtained through least-squares fitting.

Deleted: (1)
(2) in this study,(3) Comparisons between SO_2 retrievals from different fitting windows used in the literature（312-326nm (Theys et al., 2017), 310.5-326nm(Theys et al., 2021), 310.5-340nm(Li et al., 2013), 308-333nm（Yang et al., 2009; Yang et al., 2013)，312-330nm (Nowlan et al., 2011)）over the Sundhnúkur volcano and its surrounding clean region for August 23, 2024 (Fig. 2) show that the retrieval results from the 312–326 nm fitting window have higher SO2 values in the volcanic region, and exhibit lower standard deviations and mean values in the clean regions (cross-track positions 1-150). 也就是说，demonstrate the advantage 可行性 of the 312-326 nm fitting window for OMS SO_2 retrievals。The four discrete retrieval wavelengths (310.8, 311.9, 313.2, and 314.4 nm) used by Band Residual Difference (BRD) algorithm (Krotkov et al., 2006) are not included in this study due to the OMS SO2 DOAS retrieval using a continuous UV fitting window for SO_2 retrieval. The 300-335 nm fitting window used by the EISF algorithm (Yang et al., 2010) also was not included in this study because the OMS VIS spectral band starts from 307 nm and the OMS UV2 spectral range from 300 nm to 320 nm requires further calibration.
In this study, the 312-326 nm fitting window was chosen for the SO_2 retrieval from OMS observations. This is mainly based on the following considerations:
(1) Firstly, in the wavelength range 310-330 nm, although SO_2 has stronger absorption at shorter wavelengths (Fig. 1) which would make it preferable, satellite measurements at shorter wavelengths have lower SNR, and in the case of volcanic SO_2 emission, the TOA reflected radiances are prone to saturation which leads to underestimation of volcanic SO_2. Therefore, it is not appropriate to select the fitting window with the strongest SO_2 absorption for SO_2 retrieval.
(2) Secondly, longer UV wavelengths, due to the weaker absorption of SO_2, tend to introduce more noise into the retrieval of the SO_2 column. This is because the weaker absorption may make it more difficult to accurately distinguish the SO_2 absorption information from background noise and interference of O_3 absorption, especially in the case of low SO_2 emissions from anthropogenic sources.
(3) Thirdly, selecting the 312–326 nm fitting window makes the OMS SO_2 product consistent with the widely used TROPOMI SO_2 product (Theys et al., 2017). However, in this study, we did not adopt a strategy with multiple fitting windows for different SO_2 concentration conditions as is used in the TROPOMI product.
(4) Finally, in order to demonstrate the advantage of the 312-326 nm fitting window for OMS SO_2 retrievals, comparisons were conducted between SO_2 retrievals from different fitting windows over the Sundhnúkur volcano and its surrounding clean region for August 23, 2024 (Figs. 2, 3, and 4). Note that negative values often appear in SO_2 retrievals, and small negative values can indicate low SO_2 emissions in clean areas. In this study, all SO_2 retrievals greater than -10 DU are selected for comparison to exclude obvious outliers. The details of the comparisons are described below.
The main fitting windows and retrieval algorithms used in the literature for SO_2 retrievals based on ultraviolet hyperspectral satellite measurements are listed in Table 2. The OMS SO_2 columns retrieved using these different fitting windows are shown in Figs. 2, 3, and 4. Note that due to the DOAS algorithm generally using a continuous UV fitting window for SO_2 retrieval, the OMS SO_2 results from BRD four discrete wavelengths (310.8, 311.9, 313.2, and 314.4 nm) at absorption peak and valley (Krotkov et al., 2006) are not included in this study. It also should be noted that, since the OMS VIS spectr...

Deleted: FY3F/OMS

Table 2. Parameter settings for the retrieval of FY-3F/OMS SO_2 SCD

Parameter	FY-3F/OMS SO_2 DOAS settings
Retrieval fitting window	312－326 nm
Solar irradiance	TSIS-1 HSRS hybrid solar reference spectrum (Coddington et al., 2021)
Cross-sections	SO_2 273K (Bogumil et al., 2003) O_3 223K (Bogumil et al., 2003)
Ring effect	Ring spectrum calculated using the SCIATRAN model at SZA=30°, VZA=0°, RAA=0°, AS=0.05, Clear sky (Rozanov et al., 2005)
Polynomial	3th order
Background offset correction	Iterative and sliding correction scheme

3.4 AMF

The reflected radiance detected by the satellite instrument contains information of trace gases integrated along the slant observation path. From the reflected radiance and above DOAS spectral fitting, the SO_2 SCD can be derived; however, the SCD is not suitable for the application of satellite-derived SO_2 in monitoring global climate change and air pollution, as it represents the SO_2 column along the slant path, which is influenced by the observation geometry and atmospheric conditions. The SCD can be converted to VCD using AMF=SCD/VCD (Palmer et al., 2001), which represents the relative length of the mean slant path at a certain wavelength for photons interacting with a certain absorber in the atmosphere relative to the vertical path (Lorente et al., 2017).

The AMF can be expressed as a function of these parameters:

$$\mathrm{AMF} = f(\mathrm{SZA}, \mathrm{VZA}, \mathrm{RAA}, \mathrm{AS}, \mathrm{HS}, S(z), O_3, \lambda, \mathrm{clouds}, \mathrm{aerosols}) \quad \text{(Eq. 2)}$$

Where AS is the surface reflectance, HS is the terrain height, $S(z)$ represents the SO_2 vertical profile shape, O_3 is total ozone column. In practice, the AMF is typically computed as the weighted average of altitude-dependent Box-AMFs (equivalent to scattering weights) across all layers, with the weights determined by the SO_2 distribution in each layer (Eq. 3) (Chen et al., 2009; Wagner et al., 2007; Palmer et al., 2001; Boersma et al., 2004):

$$\mathrm{AMF} = \sum_i \text{Box-AMF}_i \times \frac{c_i \cdot \Delta h_i}{\sum_j c_j \cdot \Delta h_j} \quad \text{(Eq. 3)}$$

Where c_i represents the SO_2 number density in the i-th layer, and Δh_i denotes the thickness of that layer. Box-AMFs quantify the contribution of each atmospheric layer to the total AMF and allows for flexible updates of AMF with new SO_2 profiles, eliminating the procedure of rebuilding the AMF lookup table (LUT).

Deleted: 3

Deleted: FY3F/OMS

Deleted: FY3F/OMS

Deleted: 3.4 Background offset correction
The retrieval accuracy of SO_2 columns from satellite measurements is usually affected by spectral and radiometric calibration errors, which are difficult to remove from L1 radiance data and result in systematic biases in the retrieval results, such as along-track stripes and cross-track asymmetry (Boersma et al., 2004). In addition, due to the low SNR of measurements in the fitting window, the weak SO_2 absorption information included in the TOA reflected radiance, and the interference from strong O_3 absorption in the fitting window, the OMS SO_2 retrievals tend to be systematically overestimated or underestimated over the whole orbit. These systematic biases in the retrieval results of SO_2 columns are mixed with the absorption information of SO_2 and limit the applicability of the OMS SO_2 product. Therefore, it is necessary to apply a background offset correction to reduce these systematic biases in the retrieved SO_2 columns. The reference region method (Khokhar et al., 2005; Richter et al., 2006) was used to correct the background offsets, which are latitude-dependent and related to the cross-track position. This method selects retrieval values over a reference region (e.g., clean oceanic Pacific regions, assumed to be areas with no SO_2) as the background area. The SO_2 retrievals are then adjusted by subtracting the background offsets of the same latitude over the ocean. Yang proposed the sliding median correction method (Yang et al., 2007) and applied it to the OMI SO_2 product. This method performs averaged sampling within a sliding window centered on the pixel (selecting pixels with values less than 2 DU) to get background offsets for each row of pixels. With the sliding window method, the cross-track and along-track biases varying with time and location can be effectively eliminated.
For OMS SO_2 retrievals, based on the above background offset correction methods, we developed an improved iterative sliding correction scheme to avoid seam problems due to discontinuous integration times within the same orbit. The details of the background offset correction used for OMS SO_2 retrievals are as follows.
(1) Firstly, based on the integration time of FY3F/OMS L1 data, the orbital data is divided into several data blocks corresponding to different integration times. For each data block, the mean vector (V0) at each cross-track position is estimated using all valid pixels within the block (i.e., pixels with normal L1 data, as indicated by the L1 QA quality flag). Each scan line within the data block is processed by subtracting V0 from the SO_2 retrievals of each scan line to obtain the initially corrected SO_2 columns.
(2) Secondly, based on the initially corrected SO_2 columns, the predefined SO_2 threshold (2 DU), and the sliding window, the mean vector V1 for cross-track positions within each sliding window is estimated. The initially corrected SO_2 columns are then processed by subtracting V1 to obtain the double-corrected SO_2 columns. Note that the size of the sliding window varies with the satellite's spatial resolution. In this study, for the FY3F/OMS with nadir resolution ...

Deleted: 5

Deleted: T

Deleted: 2

Deleted:

Deleted: 2

Deleted:

In this study, OMS SO_2 AMFs were calculated using Box-AMFs derived from SCIATRAN and SO_2 vertical profiles from the Goddard Earth Observing System Composition Forecast (GEOS-CF) system (Fahrland et al., 2020) (Data source: https://portal.nccs.nasa.gov/datashare/gmao/geos-cf). The GEOS-CF system combines the GEOS weather analysis and forecasting system with the GEOS-Chem chemistry module (Keller et al., 2021) to provide detailed chemical analyses of a wide range of air pollutants, including O_3, NO_2, SO_2, and $PM_{2.5}$. The GEOS-CF SO_2 vertical profiles, with a horizontal resolution of 0.25° × 0.25°, a temporal resolution of 1 hour, and 72 vertical model layers extending up to 0.01 hPa, were temporally matched to the OMS overpass time and spatially interpolated to the center of each OMS pixel. The profiles were normalized and used as weighting functions in the AMF calculation.

To improve computational efficiency, a cloud-free Box-AMF LUT was built using SCIATRAN, considering six variables: SZA, VZA, RAA, AS, HS, and O_3 column. The detailed values for each variable are listed in Table 3. Although Box-AMFs are wavelength-dependent, the LUT in this study was calculated at 320 nm, approximately at the center of the OMS SO_2 retrieval window (312–326 nm). For each OMS pixel, Box-AMF values were obtained by multi-dimensional interpolation within the LUT according to the corresponding observational geometry (SZA, VZA, and RAA) and atmospheric and surface conditions (AS, HS, and O_3). The observational geometry parameters and surface height were directly obtained from the OMS L1 radiance product. The corresponding surface reflectance was interpolated from the OMI surface reflectance climatology (Kleipool et al., 2008). The total ozone column used for LUT interpolation was obtained from the corresponding OMS ozone product (Xu et al., 2025). Due to the current unavailability of synchronized and reliable OMS cloud and aerosol products, the effects of clouds and aerosol on SO_2 retrievals were not considered in this study. Consequently, the AMFs for all OMS pixels were calculated using the cloud-free Box-AMF LUT. Section 5.2 of this study provides a detailed description of the AMF error analysis.

Table 3. Values of the six variables used in the cloud-free Box-AMF LUT

Variable	Values
SZA (°)	0, 9.3, 21.2, 32.9, 44.2, 54.9, 64.8, 73.5, 80.8, 86.1
VZA (°)	0, 9.3, 21.2, 32.9, 44.2, 54.9, 64.8, 73.5
RAA (°)	0, 30, 60, 90, 120, 150, 180
AS	0, 0.01, 0.025, 0.05, 0.075, 0.1, 0.15, 0.2, 0.25, 0.325, 0.4, 0.5, 0.6, 0.7, 0.8, 0.9, 1
HS (km)	0, 0.5, 1, 2, 3, 4, 5, 6, 7, 8, 9, 10, 11, 12
O_3 column (DU)	75, 125, 175, 225, 275, 325, 375, 425, 475, 525, 575

Deleted: (Fahrland et al., 2020)

Deleted: (Keller et al., 2021)

Deleted: (Xu et al., 2025)

Deleted: However, due to the difficulty in obtaining accurate and satellite-synchronized global SO_2 profiles, we adopted a simplified approach that uses two constant AMF values representative for typical conditions for the OMS SO_2 conversion from SCD to VCD in this study. One is AMF=1 for clean regions and non-ice/snow-covered areas influenced by anthropogenic sources and volcanic eruptions, while the other is AMF=2 for the ice/snow-covered areas. These two AMF constants are approximate values derived using the SCIATRAN Box-AMF and a 5 DU anthropogenic SO_2 profile under typical atmospheric and surface conditions (SZA = 32.9°, VZA = 0°, RAA = 0°, AS = 0.05 and 0.5, HS = 0 km, wavelength = 320 nm, a 365 DU midlatitude ozone profile (Sinnhuber et al., 2009), and with the assumption of surface reflectance as isotropic Lambertian equivalent reflector (LER)). …

Deleted: more

Deleted: Box-AMF and an

Deleted: of the AMF

Deleted:

3.5 Background offset correction

The retrieval accuracy of SO_2 columns from FY-3F/OMS is affected by spectral and radiometric calibration errors, which are difficult to remove from OMS L1 radiance data and result in systematic biases in the retrieval results, such as along-track stripes and cross-track asymmetries (Boersma et al., 2004). The TSIS-1 HSRS hybrid solar reference spectrum used in OMS SO_2 retrievals does not contain instrument-related characteristics, meaning that certain calibration errors in the radiance data cannot be cancelled out during the DOAS fitting process. This may further contribute to systematic biases in the retrieved OMS SO_2 columns. In addition, due to the low SNR of measurements in the fitting window, the weak SO_2 absorption information included in the TOA reflected radiance, and the interference from strong O_3 absorption in the fitting window, the OMS SO_2 retrievals tend to be systematically overestimated or underestimated over the whole orbit. These systematic biases in the retrieval results of SO_2 columns are mixed with the absorption information of SO_2 and limit the applicability of the OMS SO_2 product. Therefore, it is necessary to apply a background offset correction to reduce these systematic biases in the retrieved SO_2 columns. The reference region method (Khokhar et al., 2005; Richter et al., 2006) was used to correct the background offsets, which are latitude-dependent and related to the cross-track position. This method selects retrieval values over a reference region (e.g., clean oceanic Pacific regions, assumed to be areas with no SO_2) as the background area. The SO_2 retrievals are then adjusted by subtracting the background offsets of the same latitude over the ocean. Yang proposed the sliding median correction method (Yang et al., 2007) and applied it to the OMI SO_2 product. This method performs averaged sampling within a sliding window centered on the pixel (selecting pixels with values less than 2 DU) to get background offsets for each row of pixels. With the sliding window method, the cross-track and along-track biases varying with time and location can be effectively eliminated.

For OMS SO_2 retrievals, based on the above background offset correction methods, we developed an improved iterative sliding correction scheme to avoid seam problems due to discontinuous integration times within the same orbit. The details of the background offset correction used for OMS SO_2 retrievals are as follows.

(1) Firstly, based on the integration time of FY-3F/OMS L1 data, the orbital data is divided into several data blocks corresponding to different integration times. For each data block, the mean vector (V0) at each cross-track position is estimated using all valid pixels within the block (i.e., pixels with normal L1 data, as indicated by the L1 QA quality flag). Each scan line within the data block is processed by subtracting V0 from the SO_2 retrievals of each scan line to obtain the initially corrected SO_2 columns.

(2) Secondly, based on the initially corrected SO_2 columns, the predefined SO_2 threshold (2 DU), and the sliding window, the mean vector V1 for cross-track positions within each sliding window is estimated. The initially corrected SO_2 columns are then processed by subtracting V1 to obtain the double-corrected SO_2 columns. Note that the size of the sliding window varies with the satellite's spatial resolution. In this study, for the FY-3F/OMS with nadir resolution of 7 km×7 km, the sliding window is set to 200 scan lines. It is worth noting that there is a trade-off between the size of the sliding window and

the effectiveness of the offset correction: too big a window might result in poor offset correction, while too small a sliding window might lead to reduction of the SO_2 information contained in the satellite measurements.

(3) Finally, based on the double-corrected SO_2 results, the predefined SO_2 threshold, and the sliding window, an iterative procedure is performed until the relative deviation between the results of the two consecutive corrections is less than or equal to 5%.

4 Comparison of OMS SO_2 columns with TROPOMI observations

Based on the FY-3F/OMS L1 measurements and the retrieval scheme outlined in section 3, global SO_2 columns from FY-3F/OMS were retrieved and applied to monitor the SO_2 emissions from volcanic and anthropogenic activities. Evaluating the accuracy of OMS SO_2 retrievals is challenging, as it is difficult to obtain synchronous and high-quality ground-based or airborne measurements for the validation of OMS SO_2 retrievals. Therefore, in this study, due to its high spatial and spectral resolution in the UV-VIS band and its common use in global SO_2 monitoring, the TROPOMI SO_2 total column product was selected as reference to evaluate the accuracy of OMS SO_2 retrievals (Theys et al., 2019; Wang et al., 2022; Theys et al., 2017; Cofano et al., 2021; Corradino et al., 2024; Fioletov et al., 2020). It should be noted that, in the comparison between OMS and TROPOMI SO_2 results, no filtering for cloud or large SZA was applied to the OMS SO_2 data. Instead, all OMS SO_2 retrievals greater than -10 DU were selected for the comparison, since negative values often appear in SO_2 retrievals from most instruments (e.g., OMI, GOME-2, and TROPOMI), and small negative values can indicate low SO_2 emissions in clean areas (Theys et al., 2013; Fioletov et al., 2020).

TROPOMI has a local overpass time of approximately 13:30, a spatial resolution of 5.5 km×3.5 km for SO_2 and provides daily global coverage with about 14 orbits per day. Two TROPOMI SO_2 products derived from different retrieval algorithms are used for comparison in this study: one is the TROPOMI offline L2 orbital SO_2 product from the DOAS algorithm (hereafter referred to as TROPOMI DOAS or TROPOMI-D) (Data source: https://browser.dataspace.copernicus.eu/), and the other is the TROPOMI L3 grid Planetary Boundary Layer (PBL) and 7km SO_2 product from the COBRA algorithm (hereafter referred to as TROPOMI COBRA or TROPOMI-C) (Data source: https://data-portal.s5p-pal.com/products/so2cbr.html). The TROPOMI DOAS SO_2 retrieval uses multiple spectral windows, including 312–326 nm, 325–335 nm, and 360–390 nm (Theys et al., 2017), which helps mitigate saturation effects under volcanic eruptions, whereas the TROPOMI COBRA algorithm uses 310.5–326 nm as the retrieval window, where SO_2 absorption is relatively strong. The TROPOMI COBRA SO_2 product was developed by Royal Belgian Institute for Space Aeronomy (BIRA), and reduces significantly both the noise and biases present in the current TROPOMI operational DOAS SO_2 retrievals (Theys et al., 2021). The TROPOMI COBRA L3 grid product (0.022°×0.022° equal latitude-longitude grid) was generated using the HARP gridding tool from L2 data applying a Quality Assurance (QA) filter (QA>0.5) to remove low quality data. This quality filtering may leads to some gaps in the COBRA data.

Deleted: FY3F/OMS

Deleted: FY3F/OMS

Deleted: It should be noted that, in the comparison between OMS and TROPOMI SO_2 results, no filtering for cloud or large SZA was applied to the OMS SO_2 data; instead, all OMS SO_2 retrievals greater than -10 DU were selected for the comparison.…

Deleted: ~

Deleted: from two

Deleted: e

Figure 4 shows the 15-days averaged global SO_2 VCDs from OMS, TROPOMI DOAS and TROPOMI COBRA for November 1–15, 2024. OMS DOAS SO_2 VCDs were averaged using pixels with SO_2 column greater than -10 DU, while TROPOMI DOAS VCDs used pixels with QA > 0.5. Overall, the OMS, TROPOMI DOAS and TROPOMI COBRA datasets exhibit generally consistent spatial distributions, clearly identifying the major global SO_2 emission hotspots. Minor differences between the datasets can be attributed to variations in observational geometry, overpass time, and algorithmic processing. Further comparisons based on individual orbits are presented in Sections 4.1, 4.2, and 4.3. Based on these comparisons, the performance of OMS SO_2 retrievals was evaluated over clean oceanic regions, volcanic eruption regions, and anthropogenic emission regions, as marked by the red boxes in the Fig. 5.

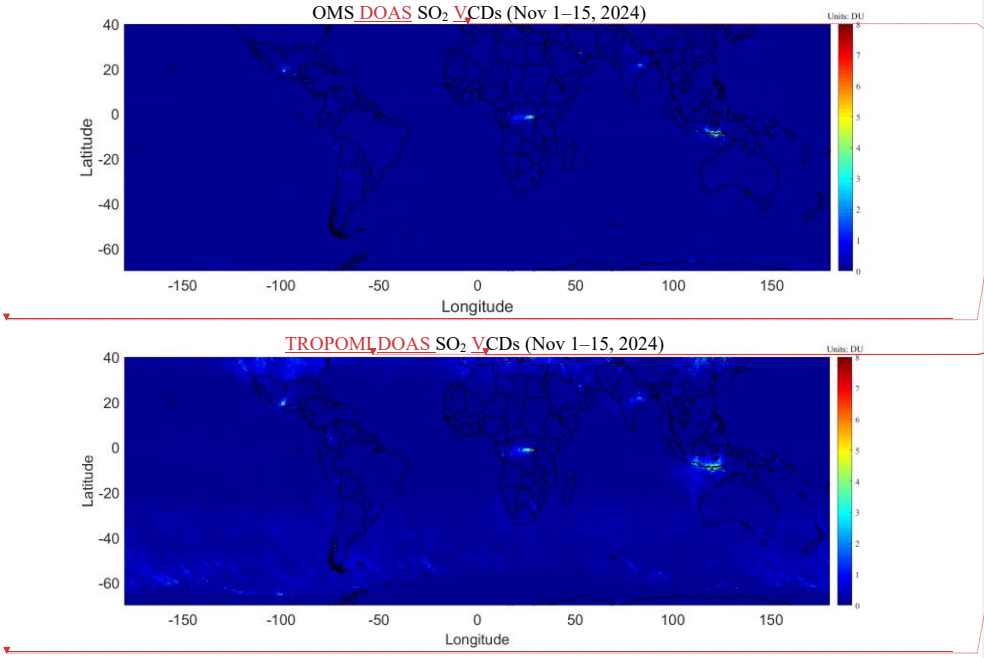

Deleted: Figure 6…shows the 15-days averaged global SO_2 …

Deleted: as shown in Fig. 7

Deleted:

…

Deleted: S

Deleted: OMS…DOAS SO_2 VS …

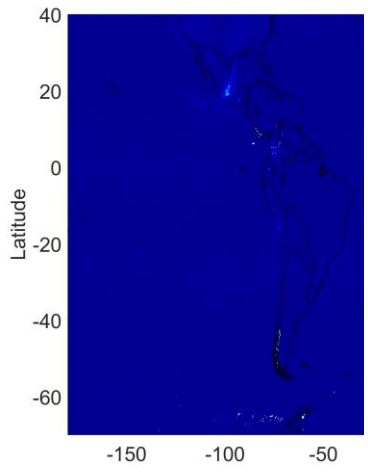

Deleted:

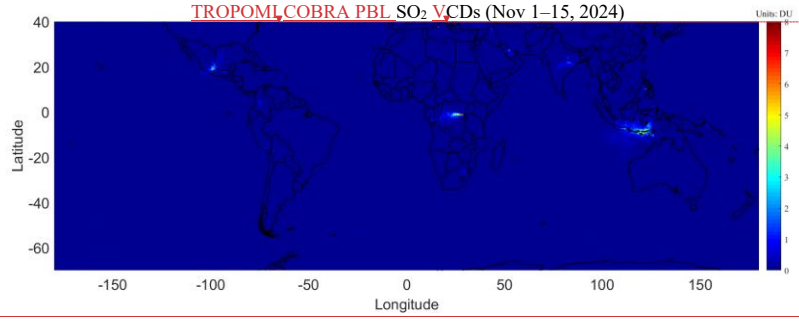

Figure 4: Global maps of averaged SO_2 VCDs from OMS, TROPOMI DOAS and TROPOMI COBRA for November 1–15, 2024, 0.2°×0.2° equal latitude-longitude grid. Note that the TROPOMI DOAS SO_2 VCDs are obtained from the product variable 'sulfurdioxide_total_vertical_column', and only pixels with QA > 0.5 are used.

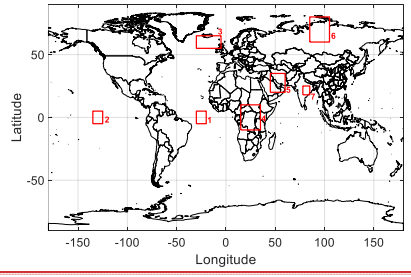

Figure 5: Regions selected for the comparison of OMS and TROPOMI SO_2 columns. Regions 1 and 2 represent clean oceanic areas, regions 3 and 4 correspond to volcanic eruption areas, and regions 5–7 represent anthropogenic emission areas.

4.1 Comparison over clean oceanic regions

Ideally, the retrieved SO_2 values from satellite observations in clean regions should be close to zero. The scatter of SO_2 columns in clean regions can reflect the reliability and stability of the satellite data and the retrieval algorithm (Krotkov et al., 2008). In this study, two clean oceanic regions, where SO_2 emissions are extremely low and assumed to be zero, were selected as the case studies to compare and evaluate the precision of FY-3F/OMS SO_2 retrievals. One is the area of latitude from 5°S to 5°N and longitude from 30°W to 20°W (Region 1 in Fig. 5), and the other is the area of latitude from 5°S to 5°N and longitude from 135°W to 125°W (Region 2 in Fig. 5). Due to the geolocation differences between OMS and TROPOMI orbits, the orbital pixels of OMS and TROPOMI DOAS and TROPOMI COBRA SO_2 product over the two clean oceanic regions were resampled to 0.15°×0.15° equal latitude-longitude grid for comparison. As suggested in the TROPOMI

Deleted: OMS
Deleted: S
Deleted: S
Deleted:
Deleted: DOAS and TROPOMI DOAS during the period of
Deleted: 1st to 15th
Deleted: SCDs
Deleted: 'fitted_slant_columns_win1'
Deleted: , corresponding to the 312–326 nm wavelength fitting window. …
. . .
Deleted:
Deleted:
Deleted: FY3F/OMS
Deleted: Ocean-Area1
Deleted: Ocean-Area2

README file, only pixels with QA > 0.5 were used for the TROPOMI DOAS SO_2 product in this section. For the cases of clean oceanic regions, TROPOMI COBRA L3 grid PBL SO_2 products were used instead of the COBRA 7km product.

As shown in Figs. 6, 7, 8, and 9, the SO_2 columns retrieved from both OMS and TROPOMI over Region 1 and Region 2 are generally low and close to zero, and they approximately follow a normal distribution centered around 0, with most values concentrated between -2 DU and 2 DU. However, there are small differences between OMS and TROPOMI SO_2 over clean oceanic regions, which become larger as the pixels approach the edge of the orbit, where retrieval uncertainties are larger. For Region 1, the standard deviations of OMS, TROPOMI DOAS and TROPOMI COBRA SO_2 columns are 0.1537 DU, 0.2493 DU and 0.1156 DU on August 23, 2024, and 0.1672 DU, 0.3934 DU and 0.1865 DU on November 15, 2024, respectively. For Region 2, the corresponding standard deviations are 0.1539 DU, 0.2636 DU and 0.1035 DU on August 23, 2024, and 0.1284 DU, 0.3595 DU and 0.1615 DU on November 15, 2024, respectively. Compared with TROPOMI DOAS SO_2 results, both TROPOMI COBRA and OMS DOAS SO_2 results show lower standard deviations and are closer to zero over Regions 1 and 2. The differences between OMS and TROPOMI SO_2 columns may be primarily related to differences in local overpass times, observation angles, L1 and L2 processing algorithms.

Overall, comparisons from different dates and different clean oceanic regions indicate that FY-3F/OMS SO_2 retrievals have a reliable precision of approximately 0.15 DU over low-emission regions, and the data quality is relatively stable over time. It is worth noting that the retrieval errors for both OMS and TROPOMI are relatively large at the edges of the orbit, which is likely due to fewer valid pixels in these regions, resulting in larger standard deviations; thus, these pixels should be used with caution.

Deleted: For OMS SO_2 retrievals, all pixels with SO_2 column greater than -10 DU are selected for comparison.

Deleted: For Ocean-Area1, both OMS and TROPOMI show low SO_2 values, and the standard deviations of OMS, TROPOMI DOAS and TROPOMI COBRA SO_2 columns over Ocean-Area1 are 0.2117 DU, 0.2468 DU and 0.1156 DU (resampling to 0.15°×0.15° equal latitude-longitude grid) on August 23, 2024, and 0.2154 DU, 0.4134 DU and 0.1865 DU (resampling to 0.15°×0.15° equal latitude-longitude grid) on November 15, 2024, respectively. For Ocean-Area2, the standard deviations of OMS, TROPOMI DOAS and TROPOMI COBRA SO_2 columns are 0.2160 DU, 0.2324 DU and 0.1035 DU (resampling to 0.15°×0.15° equal latitude-longitude grid) on August 23, 2024, and 0.2358 DU, 0.3127 DU and 0.1615 DU (resampling to 0.15°×0.15° equal latitude-longitude grid) on November 15, 2024, respectively.

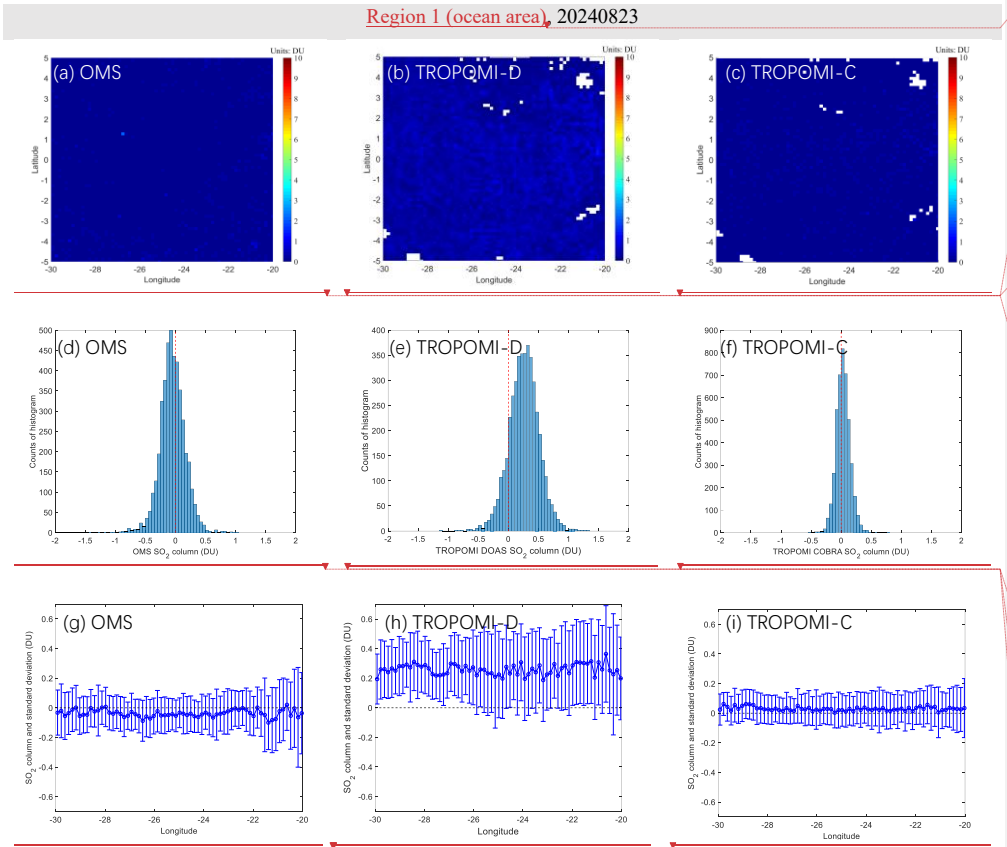

Figure 6: SO_2 retrievals over clean oceanic area (latitude from 5°S to 5°N and longitude from 30°W to 20°W, Region 1) on August 23, 2024. (a, b, c) Spatial distribution of resampled FY-3F/OMS, TROPOMI DOAS (TROPOMI-D) and TROPOMI COBRA (TROPOMI-C) PBL SO_2 columns over Region 1; (b, d, f) Histogram of resampled OMS, TROPOMI DOAS and TROPOMI COBRA PBL SO_2 columns over Region 1; (g, h, i) Variation and standard deviations of the latitude-averaged SO_2 columns over Region 1. Note that OMS pixels with SO_2 column less than -10 DU and TROPOMI DOAS pixels with QA < 0.5 are assigned the value of -9999 and are not shown in the figures. The missing pixels in Figures b and c are due to quality filtering applied to TROPOMI data.

795

Deleted: Ocean-Area1

Deleted:

Deleted:

Deleted:

Deleted:

Deleted:

Region 1 (ocean area), 20241115

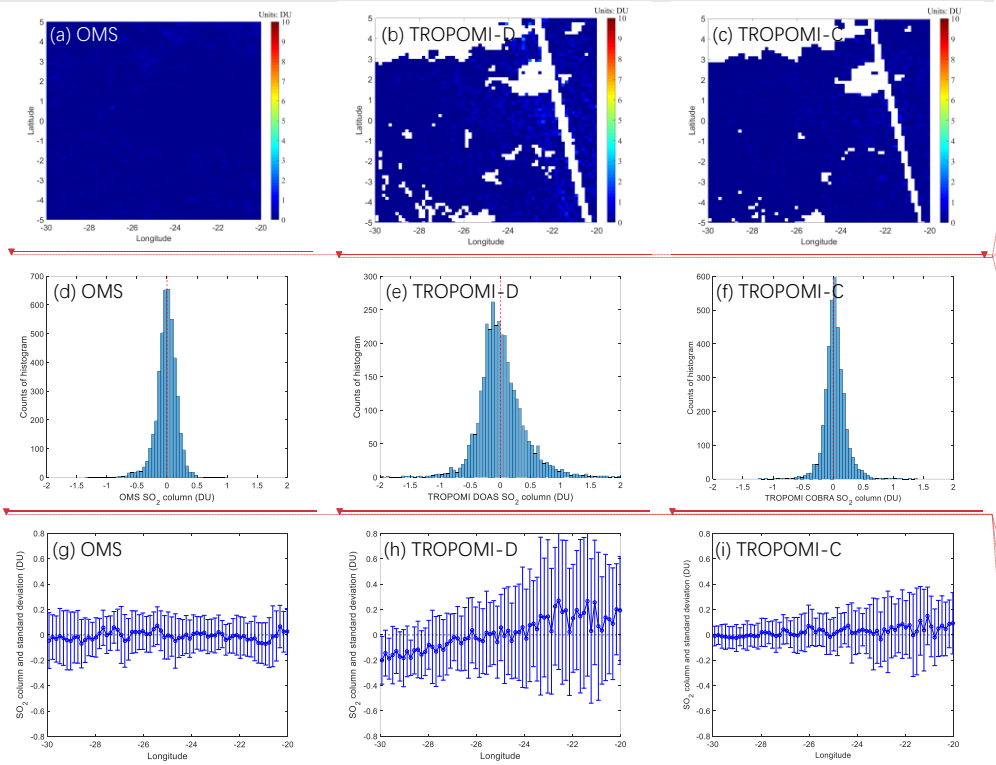

Figure 7: As Fig. 6 but for November 15, 2024. The missing pixels in Figure b and c are due to the gap between the two TROPOMI orbits, and quality filtering applied to TROPOMI data.

Deleted: Ocean-Area1

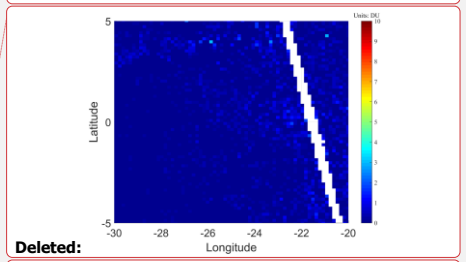

Deleted:

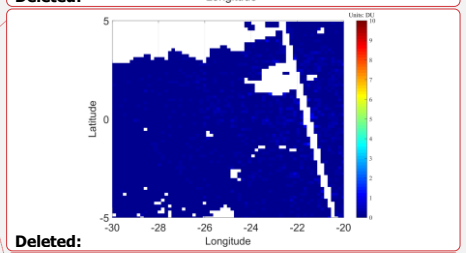

Deleted:

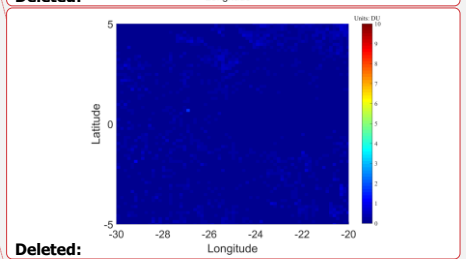

Deleted:

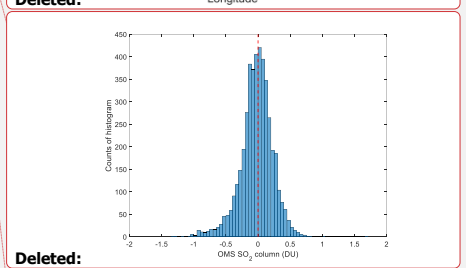

Deleted:

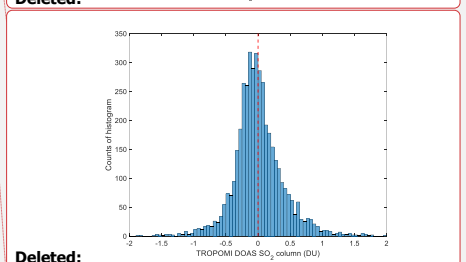

Deleted:

Region 2 (ocean area), 20240823

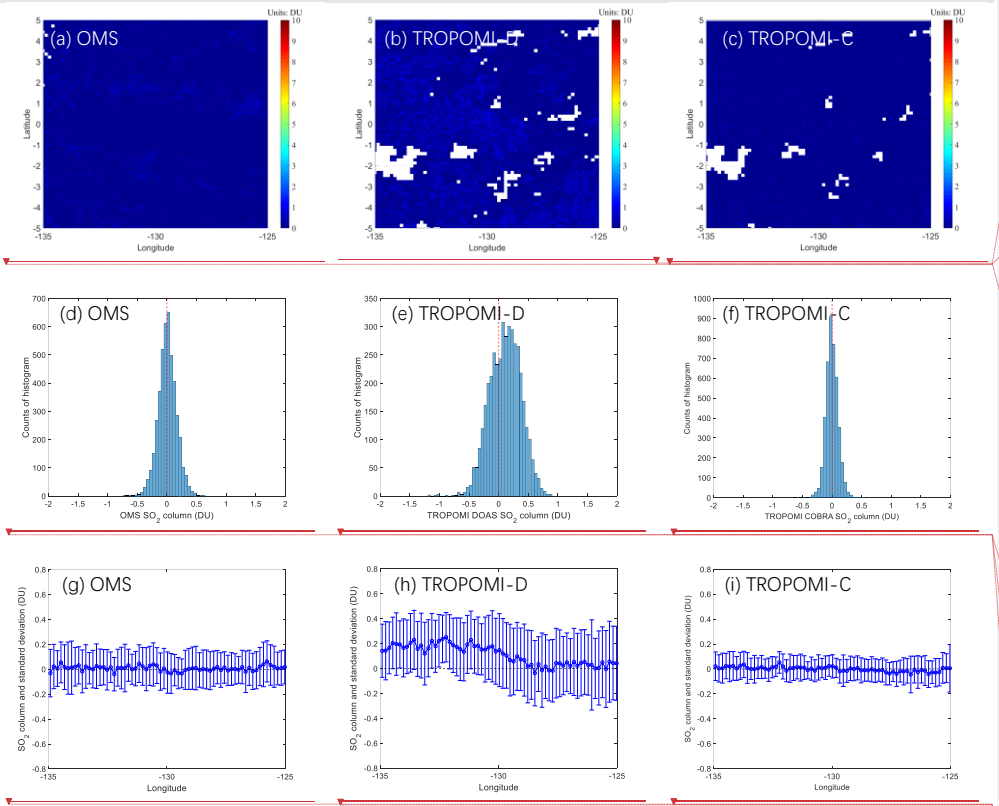

Figure 8: As Fig. 6 but for Region 2 (latitude from 5°S to 5°N and longitude from 135°W to 125°W). The missing pixels in the Figure a are caused by low spatial resolution at the edges of the orbits, and the missing pixels in the Figures b and c are caused by the quality filtering applied to TROPOMI data.

1050

Deleted: Ocean-Area2

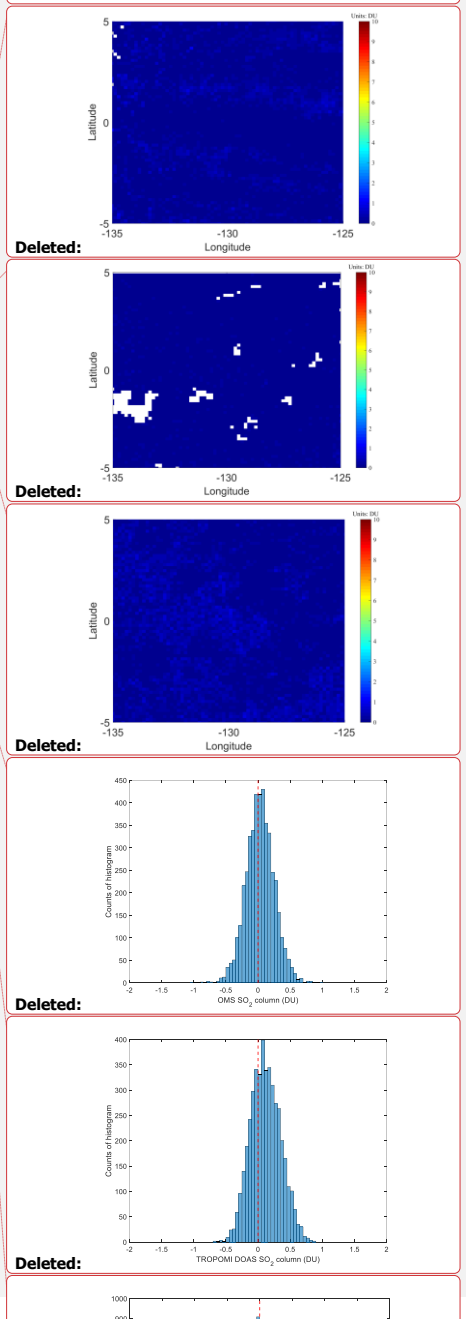

Deleted:

Deleted:

Deleted:

Deleted:

Deleted:

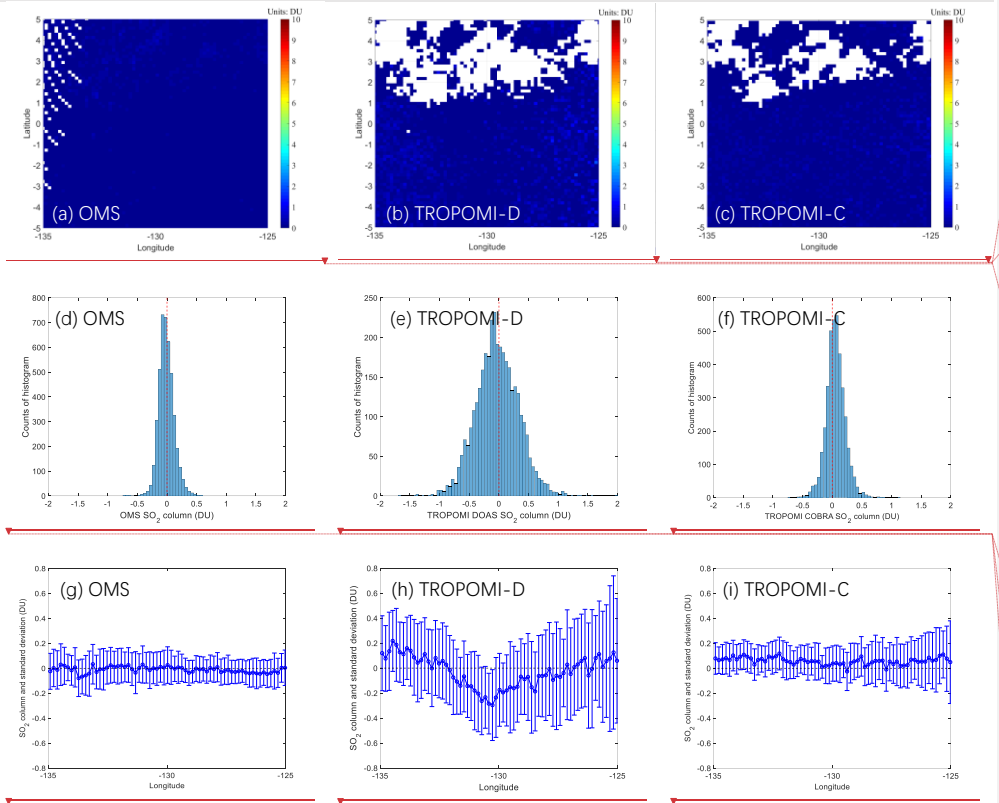

Figure 9: As Fig. 8 but for November 15, 2024. The missing pixels in the Figure a are caused by low spatial resolution at the edges of the orbits, and the missing pixels in the Figures b and c are caused by the quality filtering applied to TROPOMI data.

4.2 Comparison over volcanic eruptions

The massive amounts of SO_2 released over a short period during volcanic eruptions, as well as their long-distance transport and the subsequent formation of sulfate aerosols, not only influence the global radiative energy balance (Mccormick et al., 1995) but also pose risks to aviation in the tropopause or stratosphere (Miller and Casadevall, 2000). Through the

Deleted:

Deleted: Ocean-Area2

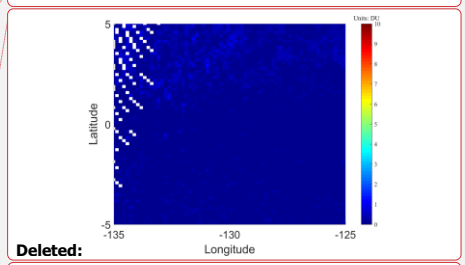

Deleted:

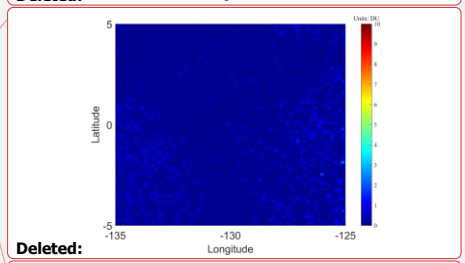

Deleted:

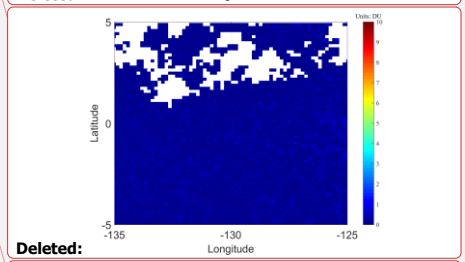

Deleted:

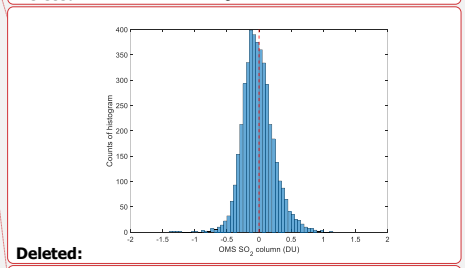

Deleted:

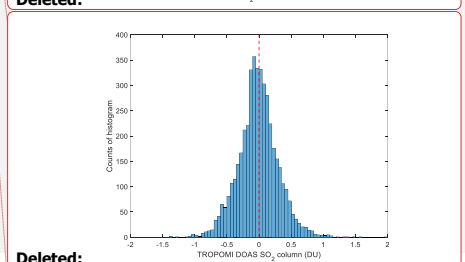

Deleted:

comparison in volcanic regions, the capability of OMS SO_2 retrievals at large columns can be evaluated. In this section, we took the eruptions of Sundhnúkur volcano (Region 3 in Fig. 5) and Nyamuragira volcano (Region 4 in Fig. 5) as case studies for comparing FY-3F/OMS SO_2 with TROPOMI DOAS and TROPOMI COBRA 7km SO_2 results. To present the SO_2 maps of OMS and TROPOMI DOAS more clearly, the resampling scheme in section 4.1 was not used in section 4.2. For TROPOMI DOAS, we used all pixels from the TROPOMI DOAS SO_2 product instead of applying QA > 0.5 to filter the high-quality pixels when comparing with the OMS SO_2 results. The reason is that after applying the QA > 0.5 filter, a lot of high SO_2 pixels in TROPOMI DOAS over volcanic regions would be missing (not shown here), making it difficult to compare with OMS SO_2 results. In this section, TROPOMI COBRA L3 grid 7km SO_2 products were used instead of PBL products.

The Sundhnúkur volcano (Region 3 in Fig. 5) is the first case study for comparing FY-3F/OMS SO_2 with TROPOMI DOAS and TROPOMI COBRA 7km SO_2 results over a volcanic eruption. On August 22, 2024, Sundhnúkur volcano within the Reykjanes volcanic system began erupting and continued to emit SO_2 for approximately 14 days (https://volcano.si.edu/). The eruption created a fissure approximately 3.9 km long, with lava and smoke reaching a height of about 1 km. The region of latitude from 55°N to 65°N and longitude from 30°W to 5°W was selected as the study area for the Sundhnúkur volcano. There are two OMS orbits (20240823_1036 and 20240823_1217) (Format: YYYYMMDD_HHMM, UTC time of the first scan line) overpassing the Sundhnúkur volcano region on August 23, 2024. For the OMS orbit 20240823_1217, most of the pixels covering the volcanic region are near the edge of the orbit where the measurement noise tends to be higher. For TROPOMI DOAS, although two orbits (20240823T125304 and 20240823T111134) (Format: YYYYMMDDTHHMMSS, observation start UTC time) passed over the Sundhnúkur volcano area, only orbit 20240823T125304 is presented because most of its pixels over the Sundhnúkur volcano region were near the nadir of the orbit where the data quality is higher. Compared with OMS orbit 20240823_1036, OMS orbit 20240823_1217 has a local overpass time closer to that of TROPOMI orbit 20240823T125304 in the volcanic region, making the SO_2 results of OMS orbit 20240823_1217 more consistent with those of TROPOMI orbit 20240823T125304.

As shown in Fig. 10, both OMS and TROPOMI successfully captured the high SO_2 distribution around the Sundhnúkur volcano on August 23, 2024. The spatial distributions of OMS, TROPOMI DOAS and TROPOMI COBRA SO_2 over Sundhnúkur volcano are similar, but differ at the edge of the SO_2 plume. The correlation between OMS and TROPOMI DOAS reaches ~0.78 over the Sundhnúkur volcano on August 23, 2024, while the correlation between OMS and TROPOMI COBRA reaches ~0.70. However, when SO_2 values exceed 50 DU, OMS SO_2 retrievals are significantly lower than those of TROPOMI DOAS over the Sundhnúkur volcano region on August 23, 2024. Moreover, the relative biases between OMS and TROPOMI DOAS increase with increasing SO_2 columns. This may be attributed to the reason that the OMS SO_2 retrieval uses the 312–326 nm fitting window, where SO_2 has strong absorption and is prone to saturation in the case of high SO_2 concentrations, leading to an underestimation of SO_2 columns. In order to mitigate the risk of saturation, TROPOMI DOAS uses two additional fitting windows (325–335 nm and 360–390 nm) (S5P-BIRA-L2-ATBD-400E) for volcanic eruption cases. In addition, the different overpass time of OMS and TROPOMI, along with varying volcanic eruption

Deleted: FY3F/OMS

Deleted: COBRA

Deleted: FY3F/OMS

Deleted: As shown in Fig. 12, both OMS and TROPOMI successfully captured the high SO_2 distribution around the Sundhnúkur volcano on August 23, 2024. The spatial distributions of OMS, TROPOMI DOAS and TROPOMI COBRA SO_2 over Sundhnúkur volcano are similar, but differ at the edge of the SO_2 plume.…

Deleted: 87

Deleted: 6

Deleted:

strength and meteorological conditions, may also be major contributors to the differences in SO_2 columns of OMS and TROPOMI DOAS. The TROPOMI COBRA SO_2 results retrieved from the 310.5–326 nm window are also lower than those from TROPOMI DOAS, but are more consistent with those from OMS.

The Nyamuragira volcano (Region 4 in Fig. 5) is the second case study for comparing FY-3F/OMS SO_2 with TROPOMI DOAS and TROPOMI COBRA 7km SO_2 results over a volcanic eruption. Nyamuragira is Africa's most active volcano and a high-potassium basaltic shield volcano located in the eastern part of the Democratic Republic of the Congo, approximately 25 km north of Lake Kivu and 13 km north-northwest of the Nyiragongo volcano (https://volcano.si.edu/). Based on the Volcanic Explosivity Index (VEI) classification (Newhall and Self, 1982) and eruptive history reports of Nyamuragira from the Global Volcanism Program (GVP), the magnitude of Nyamuragira's eruptions can generally be classified as small to moderate. According to the GVP weekly reports, Nyamuragira had continuing eruptive activities in November 2024. The spatial distribution maps (Fig. 11) show that OMS, TROPOMI DOAS, and TROPOMI COBRA results clearly detected the high-concentration SO_2 plume from the Nyamuragira eruption, although the shape of the SO_2 plume differs due to differences in overpass time, observation angles and retrieval strategies. Compared with OMS and TROPOMI DOAS, TROPOMI COBRA shows lower SO_2 columns over the Nyamuragira volcano. Although OMS and TROPOMI DOAS exhibit more comparable SO_2 levels, the quantitative agreement between them is weaker in scatter plot comparisons (not shown). This is primarily because Nyamuragira volcano is located near the equator, unlike the high-latitude Sundhnúkur volcano, making it difficult to identify OMS and TROPOMI orbits with closely matched observation times. Differences in overpass times lead to shifts in plume position, which hampers direct pixel-to-pixel quantitative comparisons over the Nyamuragira region.

Overall, from the above comparisons between FY-3F/OMS SO_2 and TROPOMI DOAS and TROPOMI COBRA 7km SO_2 results, we can see that FY-3F/OMS has the capability to monitor volcanic activities, and with high spatial resolution of 7 km×7 km and a local overpass time different from TROPOMI, FY-3F/OMS can contribute to a more effective satellite SO_2 product for the continuous monitoring of global volcanic activity.

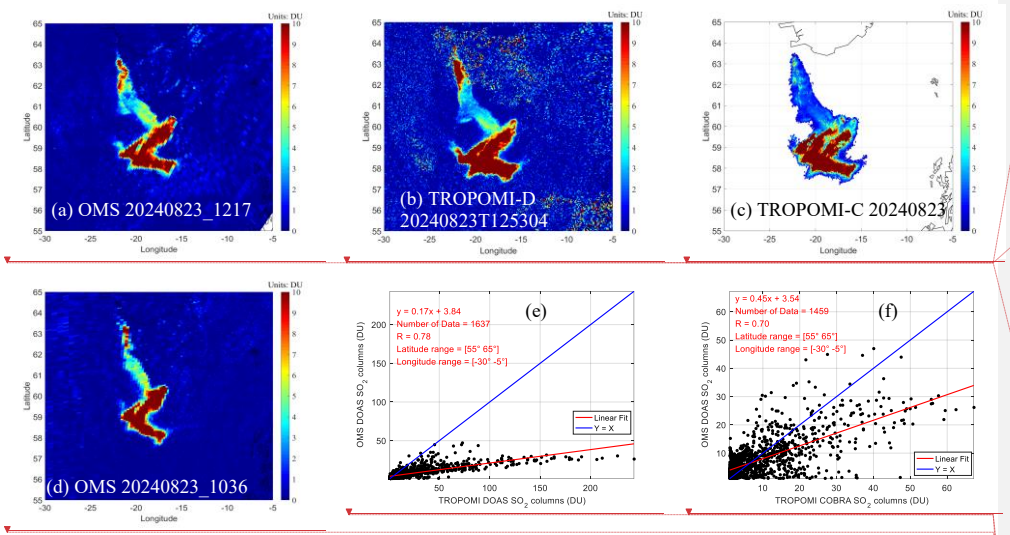

Figure 10: SO_2 retrievals over Sundhnúkur volcano on August 23, 2024. (a, b, c, d) Spatial distribution of FY-3F/OMS, TROPOMI DOAS and TROPOMI COBRA 7km SO_2 columns over Sundhnúkur volcano; (e, f) Scatter plots of OMS 20240823_1217 and TROPOMI over Sundhnúkur volcano on August 23, 2024, where pixels with SO_2 columns greater than 1 DU were selected and TROPOMI is resampled to the latitude-longitude grid of OMS. The missing pixels in Figure a are the gap between the two OMS orbits, and the missing pixels in Figure c are Nan values due to quality filtering applied to TROPOMI COBRA data.

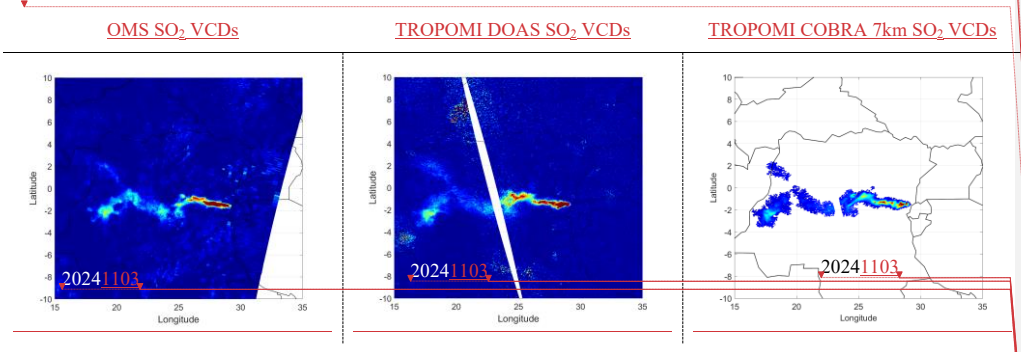

Deleted:

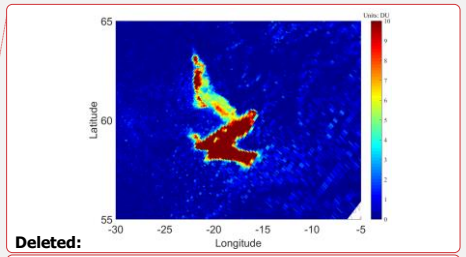

Deleted:

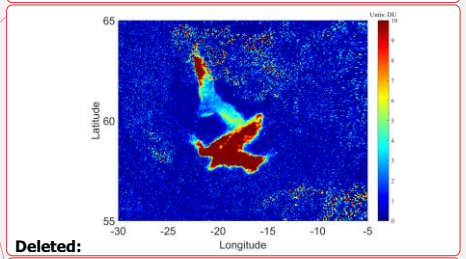

Deleted:

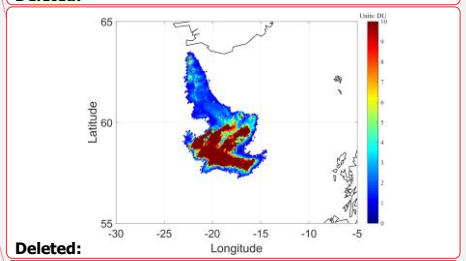

Deleted:

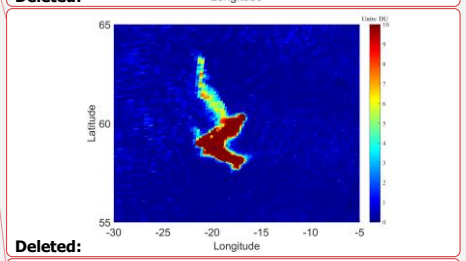

Deleted:

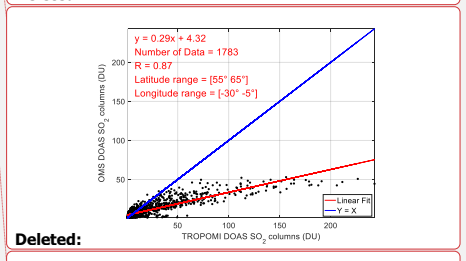

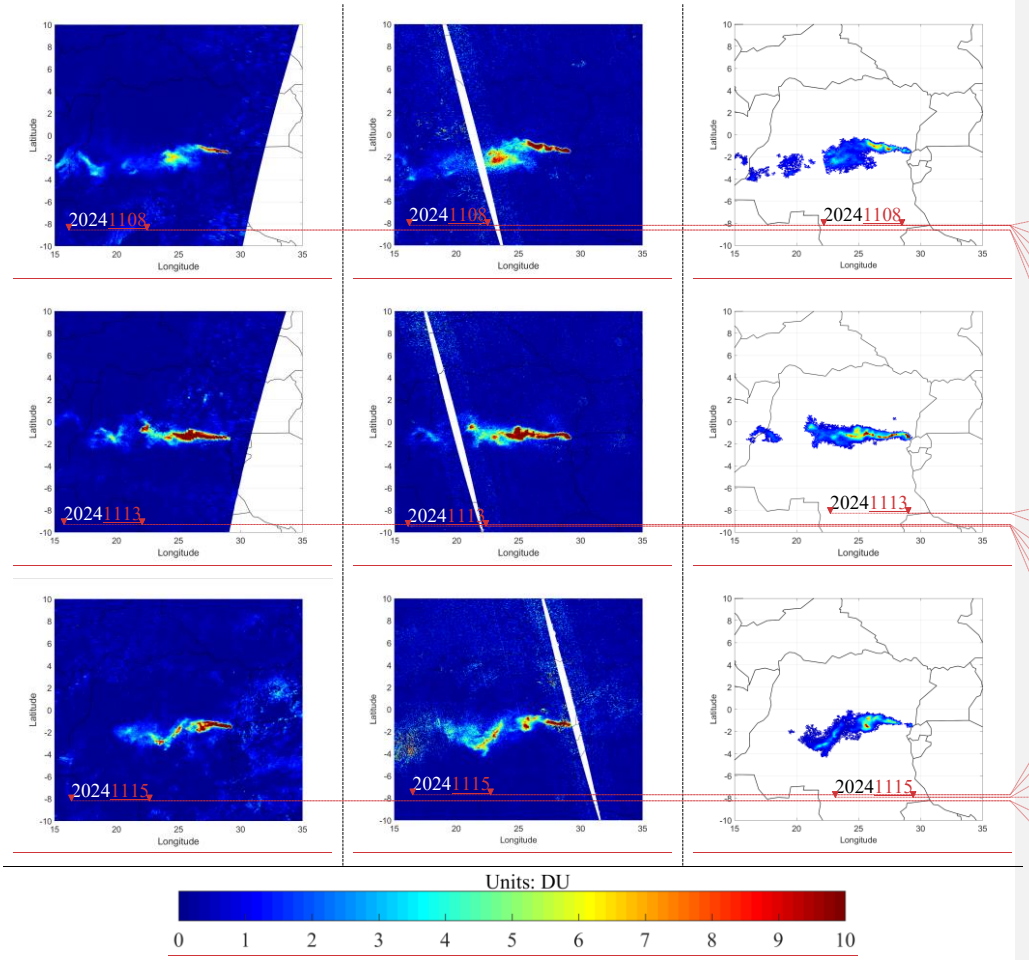

Figure 11: SO_2 retrievals of OMS and TROPOMI over the Nyamuragira volcano on November 3, 8, 13, and 15, 2024. From left to right, the panels show OMS SO_2 VCDs, TROPOMI DOAS SO_2 VCDs, and TROPOMI COBRA 7km L3 SO_2 VCDs. The missing pixels are the gap between the two orbits, or the Nan values due to quality filtering applied to TROPOMI COBRA data.

Deleted: (d) OMS
Deleted: 0823_1036
Deleted: (d) OMS
Deleted: 0823_1036
Deleted: (d) OMS
Deleted: 0823_1036
Deleted: (d) OMS
Deleted: 0823_1036
Deleted: (d) OMS
Deleted: 0823_1036
Deleted: (d) OMS
Deleted: 0823_1036
Deleted: (d) OMS
Deleted: 0823_1036
Deleted: *<object>*

4.3 Comparison over anthropogenic emissions

Compared to the monitoring of high SO_2 emissions from natural sources such as volcanoes, the monitoring of anthropogenic SO_2 emissions from satellite observations is more challenging. The atmospheric SO_2 from anthropogenic emissions is generally much lower compared to that of volcanic eruptions, and is primarily concentrated near the surface. The sensitivity of satellite measurements in the UV band near the surface is relatively low because solar UV radiation is partially absorbed and scattered by atmospheric components such as air, aerosols, and clouds during its transmission. As a result, the weakened UV radiation reaching the boundary layer reduces the sensitivity of satellite instruments to PBL SO_2 and makes it harder to distinguish SO_2 signals from background noise, especially at large solar zenith and satellite viewing angles.

Based on the SO_2 emission sources observed by TROPOMI in 2018 (Fioletov et al., 2020), we selected three representative regions – the Persian Gulf (oil and gas exploration, Region 5 in Fig. 5), Norilsk (smelters, Region 6 in Fig. 5), and Eastern India (power plants, Region 7 in Fig. 5) – to compare three SO_2 column products: OMS SO_2, TROPOMI DOAS SO_2, and TROPOMI COBRA PBL SO_2. These comparisons aim at evaluating the capability of OMS in monitoring SO_2 emissions from anthropogenic sources. Similar to the cases of volcanic eruptions, we used all pixels from the TROPOMI DOAS SO_2 product instead of applying QA > 0.5 to filter the high-quality pixels because the QA > 0.5 filter would remove many high SO_2 pixels over anthropogenic emission regions, especially over snow/ice surfaces such as Norilsk. Meanwhile, comparison results for the Persian Gulf and Eastern India regions during the study period show negligible differences whether the QA > 0.5 filter is applied or not (not shown here). In the case of anthropogenic emissions, TROPOMI COBRA L3 grid PBL SO_2 products were used for comparison instead of the COBRA 7km SO_2 products.

The Persian Gulf was selected due to its high anthropogenic emissions, including SO_2 and NO_2, primarily from oil and gas extraction and refining industries (Mardani et al., 2025; Krotkov et al., 2016). This region has a higher probability of clear-sky days and is located in the low-latitude zone, which means relatively high SNR for satellite observations. As shown in Fig. 12, OMS effectively detects high SO_2 values over the Persian Gulf while maintaining a lower background noise. The variability of enhanced SO_2 columns from OMS are generally consistent with those from TROPOMI DOAS and TROPOMI COBRA. Differences are mainly manifested in magnitude and local-scale variability, which may be attributed to differences in satellite overpass time, retrieval algorithms, AMF, and spatial resolution. Based on the spatiotemporal distributions shown in Fig. 12, three representative days with relatively large and small differences (August 23 and November 4 and 8, 2024) were selected for scatter plot comparisons among the three datasets (OMS SO_2, TROPOMI DOAS SO_2, and TROPOMI COBRA PBL SO_2). Scatter plots (Fig. 13) comparing OMS SO_2 with TROPOMI DOAS and TROPOMI COBRA SO_2 over the Persian Gulf show that: (1) Both TROPOMI DOAS and TROPOMI COBRA SO_2 products exhibit clear positive correlations with OMS, with correlation coefficients (R) ranging from ~0.63 to 0.91. (2) The level of agreement among the three datasets varies with time. On November 4 and 8, OMS shows good consistency with both TROPOMI products, with regression slopes close to unity (DOAS: slopes $\approx$ 1.00 and 0.98, R = 0.82 and 0.91; COBRA: slopes $\approx$ 0.93 and 0.96, R = 0.82 and 0.83), indicating good agreement under anthropogenic SO_2 conditions. However, on August 23, OMS retrieves

Deleted: for

Deleted: Firstly, t

Deleted: SO_2

Deleted: . Secondly,

Deleted: SO_2 from anthropogenic emission

Deleted: However, t

Deleted: .

Deleted:

Deleted: s

Deleted: 15 and 16

Deleted: SO_2

higher SO_2 columns over the Persian Gulf emission hotspot region than both TROPOMI DOAS and COBRA, with regression slopes of ~1.61 and 2.14, respectively. This discrepancy may be primarily attributed to the relatively low AMFs calculated using GEOS-CF profiles and OMI surface reflectance climatology over these high-SO_2 regions. As shown in Fig. 14, although the corresponding OMS SCD results on August 23 is relatively low, the low AMFs over region with high SCDs lead to enhanced VCD (VCD=SCD/AMF), resulting in higher OMS SO_2 VCDs over these high-SO_2 regions on August 23. (3) For pixels with low SO_2 columns, the correlations among the three datasets are relatively weak, likely due to larger retrieval uncertainties associated with random noise and reduced sensitivity at low SO_2 conditions. It should be noted that Fig. 13 does not present results for consecutive days. This is mainly due to the unavailability of GEOS-CF data for some days, the presence of a large number of pixels located near the satellite swath edges, and/or extensive cloud coverage indicated by the Terra/MODIS true color images, which limit the reliability of the comparison among the three SO_2 datasets. Similar limitations also exist in the India case studies presented later.

Norilsk in northern Russia, located within the Arctic Circle, is one of the world's biggest sources of anthropogenic SO_2 emissions due to its massive nickel and metal smelting industry (Bauduin et al., 2014). With winter lasting 6 to 9 months and snow covering the ground for most of the year, the region's low temperatures and atmospheric stability hinder pollutant dispersion, leading to persistently high SO_2 concentrations over Norilsk. Large SO_2 emissions cause severe air pollution and acid rain, which make Norilsk one of the most polluted cities in the world. On May 16, 2024, the orbits of OMS and TROPOMI with close local overpass times over Norilsk were selected to minimize the influence of emission variability and meteorological differences on the comparisons of SO_2 columns. As shown in Fig. , both OMS and TROPOMI were able to detect the high SO_2 plumes over the Norilsk region, with similar spatial patterns and transport features. The SO_2 columns from OMS and TROPOMI DOAS show strong correlations, with correlation coefficients ranging from 0.80 to 0.85 over the Norilsk region. However, OMS SO_2 VCD retrievals are lower than those from TROPOMI DOAS, with the average relative biases (|OMS - TROPOMI| / TROPOMI) of the data from the Norilsk region in OMS orbit 20240516_0334 being approximately 38% (excluding SO_2 columns smaller than 1 DU), and for OMS orbit 20240516_0516 being approximately 33% (applying the same filtering criteria). These differences may be related to differences in AMF strategy, retrieval algorithm, and spatial resolution. In contrast, the TROPOMI COBRA PBL L3 products exhibits large data gaps due to quality filtering over the Norilsk region, limiting its applicability over Norilsk for this case. In addition, the Terra/MODIS true color image from the same day shows the presence of snow cover over the Norilsk region, highlighting OMS's capability to capture anthropogenic SO_2 emissions in high-latitude regions within the Arctic Circle.

India's SO_2 emissions are mainly from coal fired power plants, transportation, and agricultural activities, which are growing rapidly, increasing by more than 100% from 2005 to 2015 (Krotkov et al., 2016; Kuttippurath et al., 2022). Eastern India, in particular, is a major hotspot due to the dense distribution of coal-based power plants and industrial facilities. As shown in Fig. 16, OMS successfully captured strong SO_2 plumes over Eastern India on 4, 5, 8, and 9 November 2024, with spatial patterns that are generally consistent with those retrieved by TROPOMI DOAS and TROPOMI COBRA. Figure 16 also includes Terra/MODIS true color images for the same days, which indicate relatively low cloud coverage over Eastern India,

Deleted: Scatter plots from different dates (August 23, 2024, and November 12, 2024) show that (1) The correlation coefficients between OMS and TROPOMI DOAS and TROPOMI COBRA SO_2 remain around 0.5–0.6; (2) TROPOMI COBRA SO_2 retrievals are lower than DOAS results over the Persian Gulf; (3) Additionally, the differences among the three datasets (OMS SO_2, TROPOMI DOAS SO_2, and TROPOMI COBRA PBL SO_2) vary over time: on August 23, 2024, OMS SO_2 retrievals were higher than those from both TROPOMI DOAS and TROPOMI COBRA, whereas on November 12, 2024, OMS SO_2 retrievals were lower than those of TROPOMI DOAS and TROPOMI COBRA. This may be attributed to the factors such as viewing angle, overpass time, local emission variations, and AMF values.…

Deleted:

Deleted:

Deleted: reduce

Deleted: impact of emission

Deleted: 17

Deleted: Note that for the OMS SO_2 retrievals over Norilsk on May 16, 2024, the constant AMF=2 was used for the conversion from SCD to VCD. …

Deleted: have a good correlation of 0.91-0.93

Deleted: In the case of Norilsk,

Deleted: slightly lower

Deleted: 2

Deleted: 2%

Deleted: outliers with relative biases greater than 200% and

Deleted: 18

Deleted: T

Deleted: which have mostly Nan values over the Norilsk region are not presented in this section.…

Deleted:

Deleted: 18

Deleted: also

Deleted: the high

Deleted: in

thereby minimizing the influence of clouds on the intercomparison of SO_2 retrievals. Despite the overall consistency in spatial distribution, OMS SO_2 retrievals over regions with strong SO_2 emissions are higher than those from TROPOMI DOAS and TROPOMI COBRA on November 5, 8, and 9, 2024. This overestimation is likely related to uncertainties in AMF calculations associated with the use of GEOS-CF SO_2 vertical profiles, OMI surface reflectance climatology, and aerosol loading over Eastern India. To further improve the accuracy of OMS SO_2 retrievals over India, future work will focus on incorporating more representative local SO_2 vertical profiles and more accurate surface reflectance databases.

Overall, the comparisons over the Persian Gulf, Norilsk, and Eastern India demonstrate that OMS SO_2 retrievals show good spatial consistency and strong correlations with TROPOMI DOAS and TROPOMI COBRA SO_2 products; OMS is capable of effectively distinguishing intense anthropogenic SO_2 signals from background noises. Owing to differences in local overpass times, OMS can provide effective complementary data to fill the monitoring gaps in TROPOMI SO_2 products.

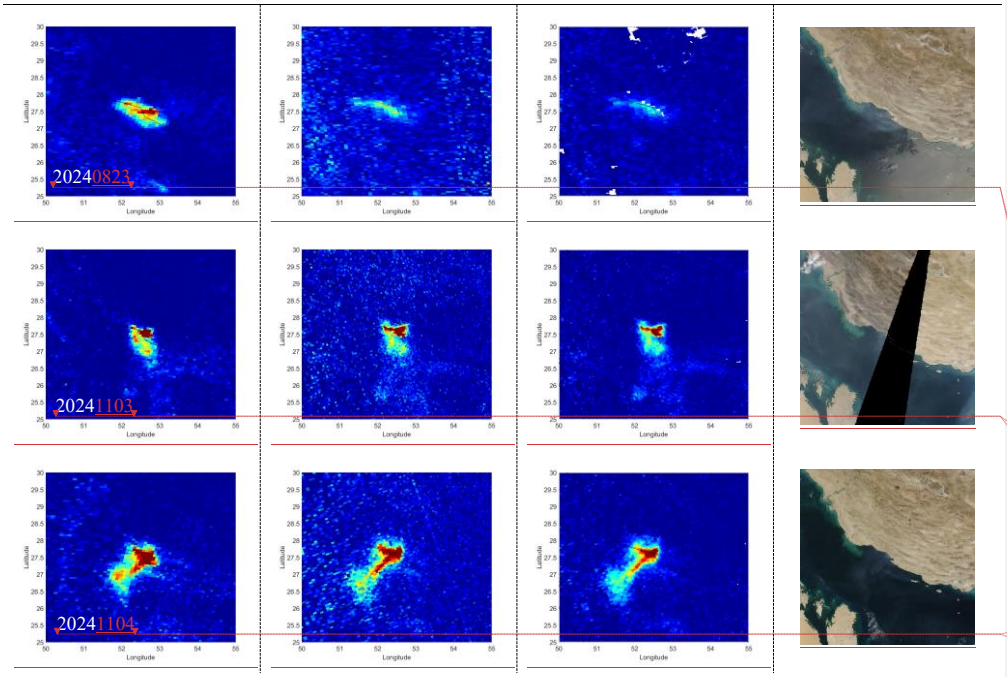

Moved down [1]: Figure 18 also shows that due to different local overpass times, when the SO_2 pollution area in India is located at the edge of the TROPOMI orbit where large retrieval errors often occur, OMS can provide effective data support to fill the monitoring gaps caused by TROPOMI's edge-related pixels. These comparisons

Moved (insertion) [1]

Deleted: , but most of OMS SO_2 retrievals are lower than those from TROPOMI DOAS. This is mainly attributed to the simplified strategy of OMS using a constant AMF=1 for the Indian region. Future work will consider using Indian local SO_2 profiles to calculate specific AMFs over India in order to improve the accuracy of OMS SO_2 retrievals over this area. It is worth noting that the ranges of the color bars in Figs. 18a1-a3 are different from others to more clearly present the OMS SO_2 retrievals over Eastern India. Figure 18 also shows that due to different local overpass times, when the SO_2 pollution area in India is located at the edge of the TROPOMI orbit where large retrieval errors often occur, OMS can provide effective data support to fill the monitoring gaps caused by TROPOMI's edge-related pixels. These comparisons demonstrate that OMS can distinguish the effective daily SO_2 information from background noises.Figure 18 also shows that due to different local overpass times, when the SO_2 pollution area in India is located at the edge of the TROPOMI orbit where large retrieval errors often occur, OMS can provide effective data support to fill the monitoring gaps caused by TROPOMI's edge-related pixels.

Deleted: (d) OMS

Deleted: 0823_1036

Deleted: (d) OMS

Deleted: 0823_1036

Deleted: (d) OMS

Deleted: 0823_1036

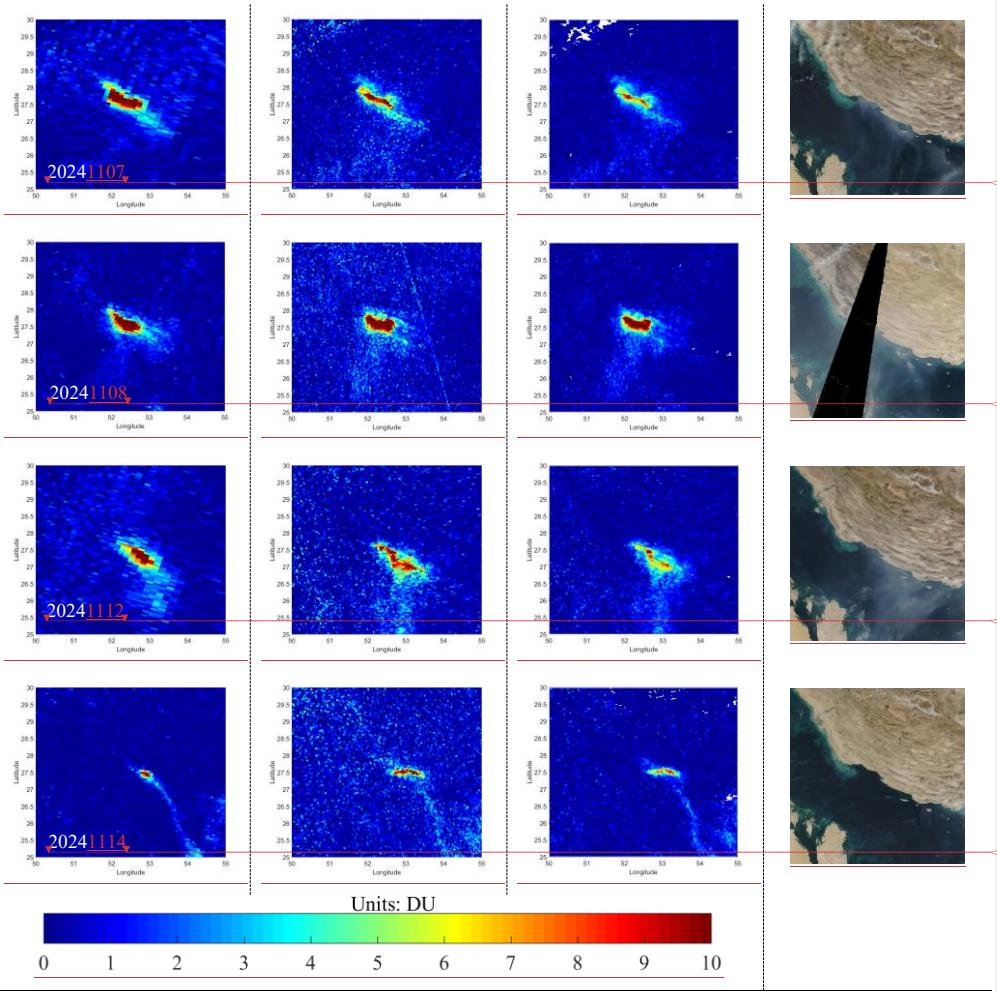

Figure 12: SO_2 retrievals of OMS and TROPOMI over the Persian Gulf on August 23, 2024, and November 3, 4, 7, 8, 12, and 14, 2024. From left to right, the panels show OMS SO_2 VCDs, TROPOMI DOAS SO_2, TROPOMI COBRA PBL L3 SO_2, and Terra/MODIS true color images. Each row corresponds to the same observation date. The missing pixels are Nan values due to quality filtering applied to TROPOMI COBRA data.

Deleted: (d) OMS
Deleted: 0823_1036
Deleted: (d) OMS
Deleted: 0823_1036
Deleted: (d) OMS
Deleted: 0823_1036
Deleted: (d) OMS
Deleted: 0823_1036
Deleted:

OMS SO_2 versus TROPOMI DOAS SO_2

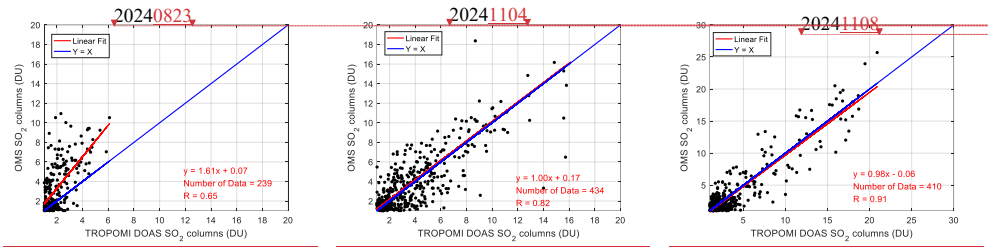

OMS SO_2 versus TROPOMI COBRA SO_2

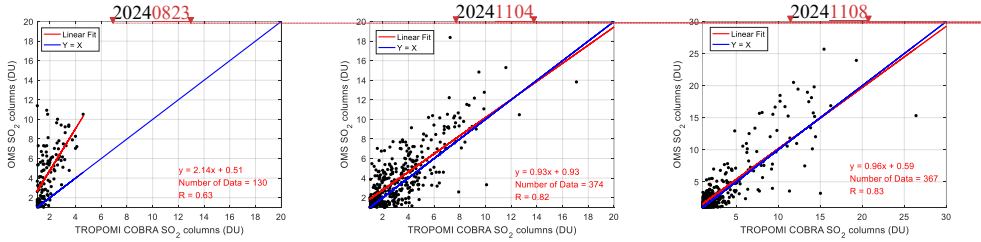

Figure 13: Scatter plots of FY-3F/OMS, TROPOMI DOAS and TROPOMI COBRA PBL SO_2 over the Persian Gulf on August 23 and November 4 and 8, 2024. Pixels with SO_2 columns greater than 1 DU were selected, and TROPOMI data were resampled to the latitude-longitude grid of OMS. Data points in the scatter plots were selected from latitude 25°–30° N and longitude 50°–55° E.

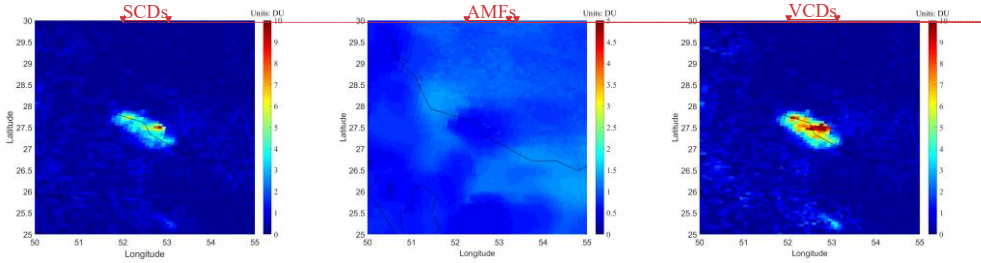

Deleted:

Deleted: (d) OMS

Deleted: 0823_1036

Deleted: (d) OMS

Deleted: 0823_1036

Deleted: (d) OMS

Deleted: 0823_1036

Deleted: (d) OMS

Deleted: 0823_1036

Deleted: (d) OMS

Deleted: 0823_1036

Deleted: (d) OMS

Deleted: 0823_1036

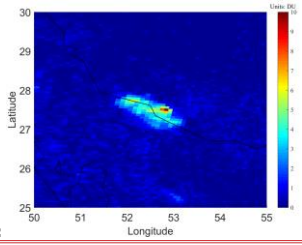

Deleted: . . .

Deleted: (d) OMS

Deleted: 20240823_1036

Deleted: (d) OMS

Deleted:

Deleted: 20240823_1036

Deleted: (d) OMS

Deleted: 20240823_1036

Figure 14: Spatial distribution of FY-3F/OMS SO_2 SCDs, AMFs, and VCDs over the Persian Gulf on August 23, 2024. VCDs=SCDs/AMFs.

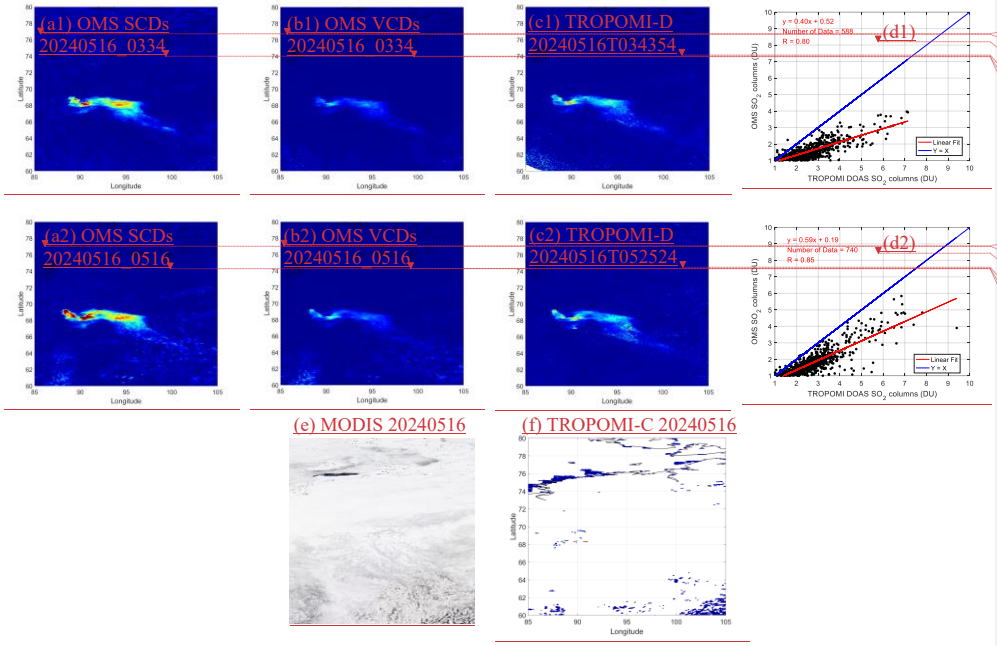

Figure 15: SO_2 retrievals over Norilsk on May 16, 2024. (a1-2, b1-2, c1-2) Spatial distribution of FY-3F/OMS and TROPOMI DOAS SO_2 columns over Norilsk; (d1-2) Scatter plots of OMS and TROPOMI DOAS SO_2 columns over Norilsk on May 16, 2024, where pixels with SO_2 columns greater than 1 DU were selected within 60–80°N and 85–105°E, and TROPOMI were resampled to the latitude-longitude grid of OMS; (e)True Color Image of Norilsk from Terra/MODIS on May 16, 2024; (f) SO_2 columns from TROPOMI COBRA PBL over Norilsk on May 16, 2024. Note that the missing pixels in Figure f are due to quality filtering applied to TROPOMI COBRA data.

Deleted:

Deleted: (d) OMS

Deleted: (d) OMS

Deleted: (d) OMS 20240823_1036

Deleted: (d) OMS 20240823_1036

Deleted: 20240823_1036

Deleted: 20240823_1036

Deleted: (d) OMS

Deleted: (d) OMS

Deleted: (d) OMS 20240823_1036

Deleted: (d) OMS 20240823_1036

Deleted: 20240823_1036

Deleted: 20240823_1036

Deleted:

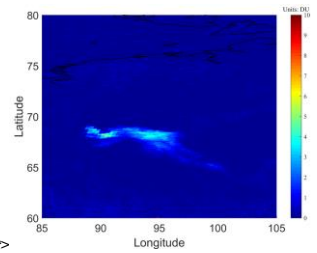

<object>

...

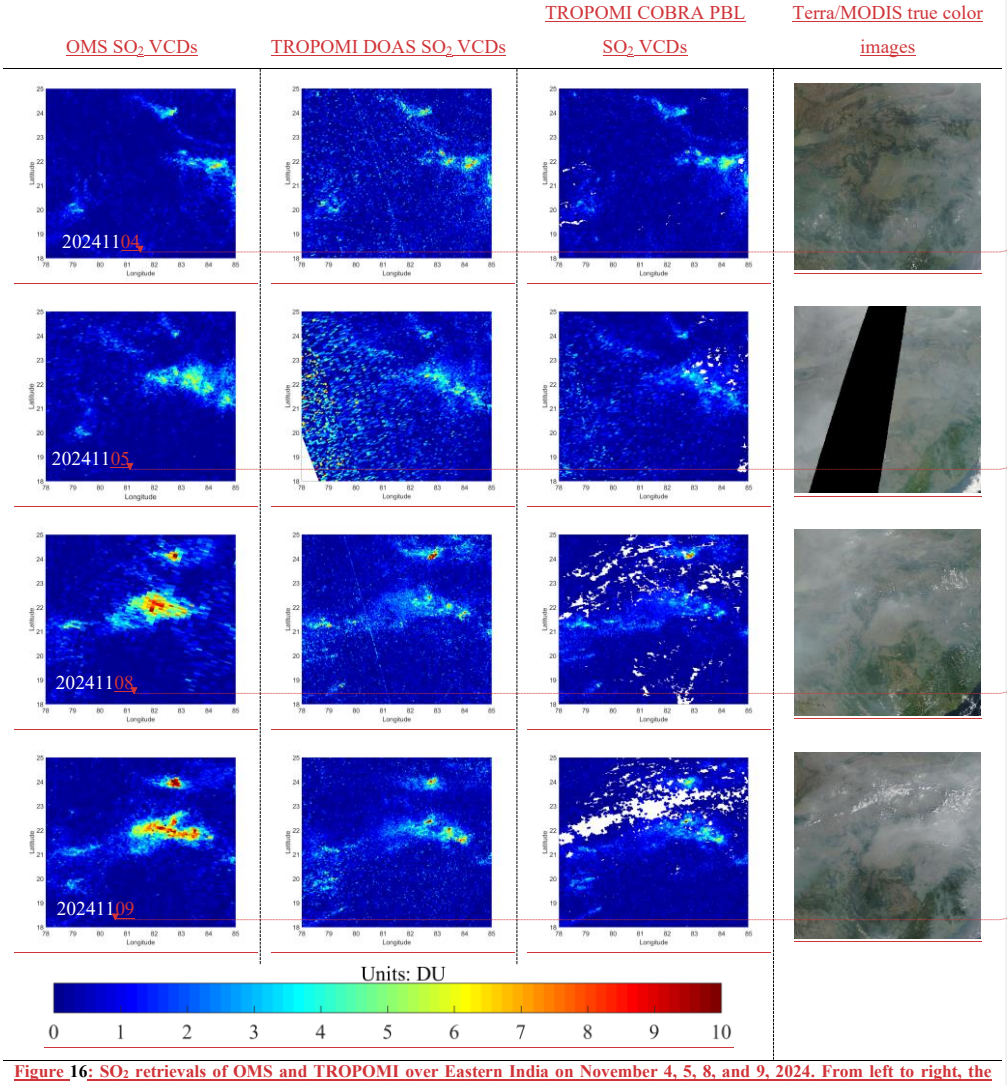

Deleted: 14

Deleted: 14

Deleted: 14

Deleted: 12

Figure 16: SO_2 retrievals of OMS and TROPOMI over Eastern India on November 4, 5, 8, and 9, 2024. From left to right, the panels show OMS SO_2 VCDs, TROPOMI DOAS SO_2, TROPOMI COBRA PBL L3 SO_2, and Terra/MODIS true color images.

Each row corresponds to the same observation date. The missing pixels are the gap between the two orbits, or the Nan values due to quality filtering applied to TROPOMI COBRA data.

5 Error analysis

The main error sources in the OMS DOAS SO_2 retrieval include instrument-related errors, DOAS SCD spectral fitting errors, AMF uncertainties, and the residual error after background offset correction (see also, e.g., Lee et al., 2009; Theys et al., 2017). Instrument-related errors include spectral and radiometric calibration errors, degradation of the instrument, stray light contamination and non-uniformity of the diffuser plate, which introduce systematic biases in both radiance and irradiance measurements. DOAS SCD spectral fitting errors include uncertainties in the absorption cross-sections of SO_2 and O_3, interference from strong O_3 absorption, the Ring effect caused by inelastic scattering, and the selection of the polynomial order in spectral fitting. The AMF, which is crucial for the accuracy of OMS SO_2 retrieval, is mainly affected by the uncertainties in surface reflectance, SO_2 vertical profile shape, wavelength dependence, and terrain height. Moreover, the background offset correction may introduce additional uncertainties, especially in high SO_2 areas.

This section is organized as follows. First, the major error sources affecting the SCD retrieval are listed, and the quantitative uncertainty of the OMS SO_2 SCD retrieval is provided. Second, the main error sources influencing the AMF are analysed, and the AMF uncertainty associated with each error component is quantitatively estimated. Third, the residual errors after background offset correction are evaluated. Finally, based on the above results, overall quantitative estimates of the uncertainty of OMS SO_2 retrieval are presented.

5.1 Errors in SCD

Table 4. Main error sources affecting the OMS SO_2 SCD retrieval

Parameter	Parameter uncertainty or resulting SCD uncertainty
OMS-N L1 absolute radiometric calibration error (requirements)	<3%
OMS-N L1 relative radiometric calibration error (requirements)	<2%
OMS-N L1 spectral calibration error (requirements)	~0.01nm
OMS-N L1diffuser calibration accuracy (requirements)	<3%
OMS-N L1 noise requirements	Signal-to-noise ratio > 250 in the wavelength range 312–340 nm
TSIS-1 HSRS reference spectrum uncertainty	~0.3%
Absorption cross-section uncertainty	~3%
Use of a fixed Ring spectrum	SCD uncertainty < 3.5%

Deleted:

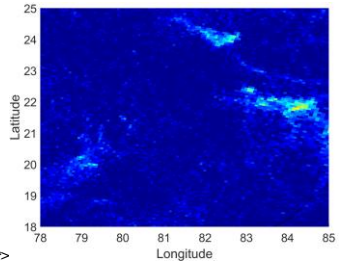

<object>

Deleted: which may introduce biases if not appropriately chosen

Deleted:

Deleted: SO_2 vertical profile,

Deleted: clouds and aerosols, and surface height

Deleted:
Considering these error sources and assuming that they are independent of each other, the total uncertainty in the retrieved SO_2 column can be approximated as:

$$\sigma_{SO_2} = \sqrt{\left(\frac{\sigma_{SCD}}{AMF}\right)^2 + \left(\frac{\sigma_{SCD}^{back}}{AMF}\right)^2 + \left(\frac{(SCD - SCD^{back}) \cdot \sigma_{AMF}}{AMF^2}\right)^2}$$

(Eq. 3)

where σ_{SCD} is the random error from DOAS SO_2 SCD spectral fitting including instrument-related noise, σ_{SCD}^{back} is the residual systematic error after background offset correction, and σ_{AMF} is the AMF uncertainty which includes two components: one is related to the atmospheric scattering weight and the other one is associated with the SO_2 profile shape.

Deleted: retrieval

Retrieval fitting window and low-order polynomial	SCD uncertainty < 11%
Others (e.g., stray light, dark current, ISRF, interference from strong O_3 absorption in the fitting window)	–

The main error sources affecting OMS SO_2 SCD primarily include instrument-related noise and algorithm settings in spectral fitting (Table 4). These error sources are difficult to separate, making it challenging to quantitatively estimate how each individual error source contributes to the SCD retrieval uncertainty. Although OMS L1 provides specified performance requirements before launch, on-orbit measurements indicate that the OMS L1 errors deviate from the planned specifications for certain parameters. At the time of writing, the updated OMS L1 errors have not yet been obtained. Therefore, in this study, we do not report the contribution of each individual error source to the final SCD uncertainty. Instead, we use the DOAS Spectral Fitting Error (SFE) to derive the overall SCD uncertainty under the current OMS L1 instrument status and DOAS settings.

5.1.1 Error source: instrument-related errors

The errors in irradiance and radiance measurements are the main instrument-related error sources affecting OMS SO_2 SCD retrievals, leading to systematic biases such as along-track stripes at specific viewing angles and cross-track asymmetry in SO_2 SCD retrievals (Boersma et al., 2004). To reduce errors related to irradiance non-uniformity, the TSIS-1 HSRS hybrid solar reference spectrum was used instead of the OMS irradiance measurements to mitigate the effects of viewing angle dependence and instrument degradation on OMS SO_2 retrieval. Radiance measurement errors mainly depend on viewing angle, wavelength, and optical degradation. The viewing angle dependence, primarily caused by calibration inaccuracies, results in unequal responses across different cross-track positions. These biases can be partially corrected using background offset correction but cannot be fully eliminated. With increasing optical degradation over the OMS on-orbit lifetime, additional errors may be introduced into the OMS radiance spectra, thereby leading to larger uncertainties of OMS SO_2 SCD retrievals.

5.1.2 Error source: absorption cross-sections

The temperature dependence and uncertainties of absorption cross-section spectra is one of the error sources which affect the accuracy of OMS SCD retrieval. The OMS SO_2 SCD retrieval utilizes the Bogumil SO_2 and O_3 absorption cross-section spectra at constant 273 K and 223 K (Bogumil et al., 2003), which is in general not representative of the effective temperature corresponding to the SO_2 vertical profile. The differences in SCD retrievals caused by temperature-dependent absorption cross-sections increase with increasing SO_2 columns (Yan et al., 2014). For example, compared to SCD retrievals using the 203 K absorption cross-sections, the differences in SO_2 SCDs can reach a maximum of ~25 DU (with SCDs around 60 DU). In addition to the temperature dependence, the uncertainties of the 273 K SO_2 and 223 K O_3 absorption cross-sections from Bogumil et al. (2003) are approximately 3.0%, which may result in ~6% systematic errors in the retrieved SO_2

Deleted: OMS

Deleted: one of

Deleted: error sources

Deleted: of

Deleted: . These errors significantly affect the accuracy of OMS SO_2 retrievals, and are the main causes of the …

Deleted: overestimation or underestimation

Deleted: of SO_2 retrievals,

Deleted: The OMS irradiance and radiance uncertainties mainly depend on viewing angle, wavelength, and optical degradation. The viewing angle dependence, caused by calibration inaccuracies, results in unequal responses for all viewing angles (one viewing angle corresponds to one cross-track position). With increasing optical degradation and inaccurate spectral calibration, more errors can be introduced into the irradiance and radiance spectra. This degradation is difficult to monitor and calibrate, because no accurate standards over the full OMS wavelength range are readily available. …

Deleted: Meanwhile, these errors in solar irradiance and earth radiance are not constant and can change with time and location, making it difficult to correct their impact on SO_2 retrievals. After one year in orbit, the intensity of OMS irradiance at the shorter wavelength of 317 nm has decreased by about 8.83%, while at the longer wavelength of 331 nm, it has decreased by about 6.07%. Using the TSIS HSRS hybrid solar reference spectrum instead of the OMS irradiance measurements can mitigate the impact of viewing angle dependence and degradation on OMS SO_2 retrieval. However, since the solar reference spectrum does not contain the instrument characteristics, it may introduce systematic overestimation or underestimation in SO_2 column retrievals. These systematic biases caused by the TSIS HSRS can be partially reduced through background offset correction but cannot be fully eliminated.

Deleted: can

Deleted: DOAS

Deleted: spectral fitting

Deleted: for DOAS SCD fitting

Deleted: However, the SO_2 and O_3 absorption cross-sections exhibit strong temperature dependence, which affects the accuracy of retrieved SO_2 SCDs when using the constant 273 K SO_2 and 223 K O_3 absorption cross-sections. The SO_2 SCD retrievals increase accordingly as higher-temperature absorption cross-sections are used (Yan et al., 2014). …

Deleted: (Yan et al., 2014)

Deleted: y

SCD within the 312–326 nm fitting window (Vandaele et al., 2009). Future work will incorporate accurate temperature correction in OMS SO_2 retrievals.

5.1.3 Error source: Ring effect

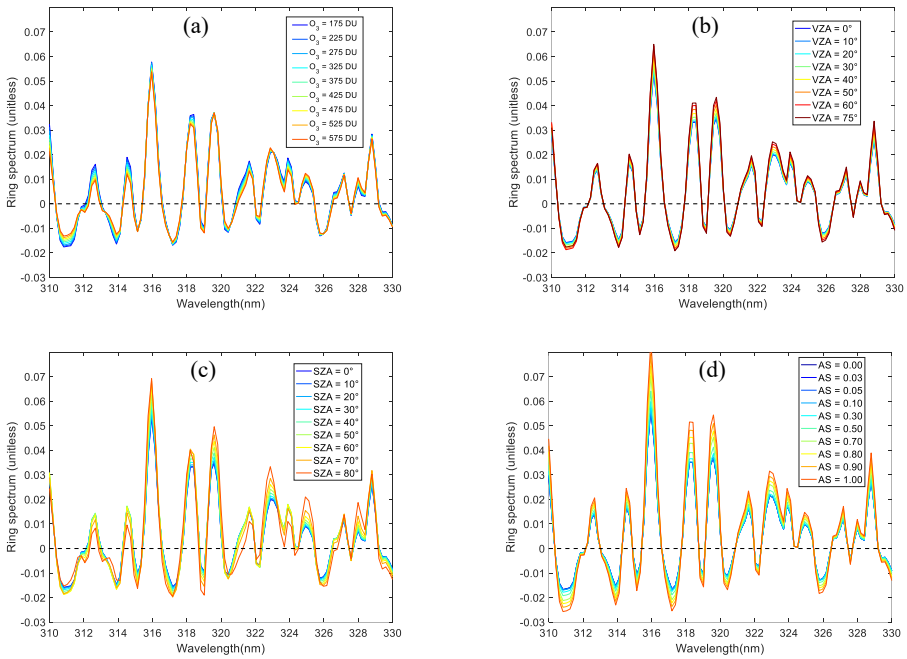

Figure 17: Variation of Ring spectrum with O_3, VZA, SZA and surface reflectivity (AS). Ring spectrum was calculated using the SCIATRAN model, convolved with the OMS ISRF. The default SCIATRAN settings for the Ring spectrum are as follows: wavelength step=0.2 nm, clear sky, HS=0 km, O_3=275 DU, AS=0.05, SZA=30°, VZA=0°, RAA=0°.

In the UV wavelength band, the Ring effect is a non-negligible part of the DOAS SCD fitting process. Taking the OMS 20240823_1036 orbit as an example, after including the Ring spectrum into the DOAS retrieval, the spectral fitting RMSE decreases by approximately 0.004 to 0.01. As shown in Fig. 17, the Ring spectrum varies with SZA, VZA, O_3 column and AS within the 310–330 nm wavelength range. The variation of the Ring spectrum with RAA is negligible and is therefore not presented. The mean percentage change in the Ring spectrum is approximately 27.67% (absolute deviation: 0.0025) as the O_3 column varies from 175 DU to 575 DU, 47.34% (absolute deviation: 0.0048) as the AS varies from 0 to 1, 24.18%

Deleted: is also one of the error sources in the SO_2 SCD retrievals. Systematic errors in slant columns due to SO_2 cross-section uncertainties are estimated to be around 6% in the 312–326 nm fitting window (Vandaele et al., 2009). The uncertainty of the SO_2 absorption cross-sections from Bogumil et al. (2003) varies with temperature, being 2.8% at 293 K and 3.0% at lower temperatures. The uncertainty of O_3 absorption cross-sections from Bogumil et al. (2003) is approximately 3.1% or less. Therefore, to improve the accuracy of OMS SO_2 retrievals, it is essential to account for the variations in the SO_2 absorption cross-section with temperature and altitude, especially in cases of volcanic eruptions. …

Deleted:

Deleted: and real-time

Deleted: and SO_2 profile data

Deleted: to account for temperature-dependent effects

Deleted: In the UV wavelength band, the Ring effect is a non-negligible part of the DOAS SCD fitting process. As shown in Fig. 19, the Ring spectrum convolved with the OMS ISRF varies with SZA, VZA, O_3 column and AS within the 310–330 nm wavelength range. The variation of the Ring spectrum with RAA is negligible and is therefore not presented. The mean percentage change in the Ring spectrum is approximately 27.67% (absolute deviation: 0.0025) as the O_3 column varies from 175 DU to 575 DU, 47.34% (absolute deviation: 0.0048) as the AS varies from 0 to 1, 24.18% (absolute deviation: 0.0021) as the VZA varies from 0° to 75°, and 45.29% (absolute deviation: 0.0047) as the SZA varies from 0° to 80°. However, in this study, a single Ring spectrum simulated with the SCIATRAN model was used to retrieve OMS SO_2 for all pixels. The reason is that although the Ring spectrum varies significantly with SZA, VZA, O_3 column, and AS within the 310–330 nm wavelength range, the impact of Ring spectrum variability on SO_2 retrievals is relatively small due to the weak correlation between the Ring spectrum and the satellite TOA reflectance, especially in the case of volcanic eruptions with high SO_2 concentrations. Moreover, using Ring spectra that vary with SZA, VZA, O_3 column, and AS within the 310–330 nm wavelength range require constructing a large lookup table, which would significantly increase computational cost for OMS SO_2 column retrievals.

Deleted: with

Deleted:
Additionally, the accuracy of DOAS SCD fitting is also influenced by the following factors: (1) Interference from strong O_3 absorption in the retrieval fitting window. Due to the overlap of O_3 and SO_2 absorption in the UV wavelength and the fact that the atmospheric O_3 absorption is often much higher than that of SO_2, the UV radiation reaching the near-surface (the primary altitude of anthropogenic SO_2 emissions) is weakened, resulting in a lower SNR. When using the weakened radiance and DOAS fitting to simultaneously retrieve O_3 and SO_2, the strong O_3 absorption signal may overshadow the SO_2 absorption information, leading to errors in the DOAS SO_2 SCD retrievals. Sensitivity analysis shows that a 1% increase in O_3 can lead to approximately a 5% decrease in DOAS SO_2 retrievals (Yan et al., 2017). (2) Selection of retrieval fitting window. Different retrieval fitting windows have varying SO_2 absorption features, O_3 absorption interference, and SNR. The scheme using a single retrieval fitting window of 312–326 nm for OMS SO_2 SCD retrieval may lead to the underestimation of SO_2 columns in …

(absolute deviation: 0.0021) as the VZA varies from 0° to 75°, and 45.29% (absolute deviation: 0.0047) as the SZA varies from 0° to 80°.

However, in this study, a fixed Ring spectrum calculated from SCIATRAN was used to retrieve SO_2 for all OMS pixels. The reason is that although the Ring spectrum varies significantly with SZA, VZA, O_3 column, and AS within the 310–330 nm wavelength range, the impact of Ring spectrum variability on SO_2 retrievals is relatively small (<3% or less) due to the weak correlation between the Ring spectrum and the satellite TOA reflectance, especially in the case of volcanic eruptions with high SO_2 concentrations. Moreover, using Ring spectra that vary with SZA, VZA, O_3 column, and AS within the 310–330 nm wavelength range require constructing a large lookup table, which would significantly increase computational cost for OMS SO_2 column retrievals.

5.1.4 Error source: others

The OMS SO_2 SCD retrieval is also influenced by the following factors: (1) Interference from strong O_3 absorption in the retrieval fitting window. Due to the overlap of O_3 and SO_2 absorption in the UV wavelength, the strong O_3 absorption signal may overshadow the SO_2 absorption information, leading to errors in SO_2 SCD retrievals. (2) Selection of fitting window. Different retrieval fitting windows have varying SO_2 absorption features, O_3 absorption interference, and SNR. The scheme using a single retrieval fitting window of 312–326 nm for OMS SO_2 SCD retrieval may lead to the underestimation of SO_2 columns in the cases of volcanic eruptions. (3) Low-order polynomial. In DOAS retrievals, low-order polynomials are used to remove slow-varying components, such as aerosol scattering and broad spectral features of absorption. In this study, a third-order polynomial was used for SCD spectral fitting. The errors introduced by this polynomial will need to be quantified.

5.1.5 Total SCD uncertainties

Taking a volcanic eruption orbit as an example (wide range of measured SCDs; orbit OMS 20240823_1036), two plots of the SCD fitting RMSE and SFE are presented. As shown in Fig. 18, both RMSE and SCD uncertainty are relatively large and exhibit pronounced striping patterns. At the right edge of the swath, the SCD uncertainty exceeds 8 DU, while at the left edge it is approximately 5–6 DU. In the middle of the swath, the SCD uncertainty is about 3–5 DU. These large SCD uncertainties are mainly associated with instrument radiometric and spectral calibration errors. Although background offset corrections can substantially reduce striping patterns in the SO_2 columns, separating the contributions of instrument-related noise and spectral fitting errors to the overall SCD uncertainty remains challenging. Ongoing improvements to the OMS L1 data are expected to reduce striping and calibration asymmetries, thereby improving the accuracy of SO_2 SCD retrievals.

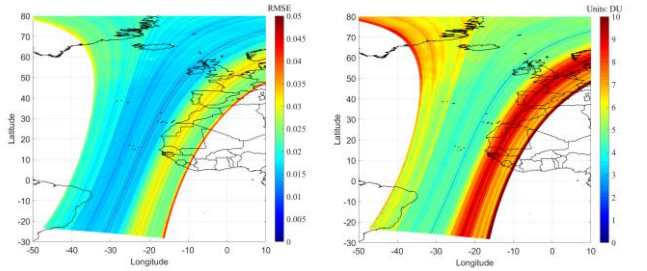

Figure 18: RMSE and SFE of OMS SO_2 SCDs for OMS orbit 20240823_1036.

5.2 Errors in AMF

AMF uncertainty is a primary source of the uncertainty of OMS SO_2 VCD retrieval. In this study, OMS SO_2 AMFs were calculated using SO_2 vertical profiles from GEOS-CF (Keller et al., 2021) and Box-AMFs derived from the SCIATRAN model (Chen et al., 2009; Wagner et al., 2007; Palmer et al., 2001; Boersma et al., 2004; see Section 3.4 for more information). The uncertainty in OMS SO_2 AMF is mainly associated with SZA, VZA, RAA, AS, HS, O_3 column, the shape of SO_2 vertical profile ($S(z)$), and wavelength (λ) dependence (Lee et al., 2009). It should be noted that the clouds and aerosols were not considered in the OMS SO_2 AMF calculation. Therefore, AMF uncertainties associated with clouds and aerosols were not included in the present AMF error analysis.

In this section, sensitivity tests of OMS SO_2 AMF were conducted using the SCIATRAN model by computing Box-AMFs under different forward-model configurations (Fig. 19). And then the contribution of each input parameter to the AMF uncertainty was quantified by perturbing it according to its estimated uncertainty while keeping other parameters fixed. Finally, an overall estimate of uncertainty in OMS SO_2 AMF was derived. For the perturbation analysis, a set of typical atmospheric and surface conditions was adopted as the default configuration, with SZA=32.9°, VZA=0°, RAA=0°, AS=0.05, HS=0 km, wavelength=320 nm, O_3 column=275 DU, clear-sky conditions, and with the assumption of surface reflectance as isotropic Lambertian equivalent reflector (LER).

The contributions of different parameters to the AMF uncertainty were evaluated across five scenarios: clean, boundary-layer pollution, boundary-layer pollution over snow and ice, volcanic degassing, and volcanic eruption. To represent these scenarios, four assumed SO_2 vertical profiles were constructed (Fig. 20), corresponding to clean conditions (SO_2 column=0.11 DU), anthropogenic SO_2 emissions (SO_2 column=5 DU), volcanic degassing with plume heights around 2 km (SO_2 column=16.5 DU), and volcanic eruptions with plume heights around 6 km (SO_2 column=120 DU).

Deleted: from

Deleted: The

Deleted: also

Deleted: one of the

Deleted: error

Deleted: s

Deleted: It can be calculated by using Box-AMF from forward radiative transfer model and local SO_2 profile (Chen et al., 2009; Wagner et al., 2007; Palmer et al., 2001; Boersma et al., 2004)….

Deleted: due to the difficulty in obtaining accurate and satellite-synchronized global SO_2 profiles, two AMF constants under typical conditions were used to convert the OMS SO_2 SCD to VCD (see section 3.5 for more information).
However, due to the heterogeneity of the global land cover and the variability of atmospheric conditions and SO_2 emission sources, the approximation using constant AMFs can introduce large uncertainties into the final SO_2 VCD retrieval.

Deleted: value

Deleted: influenced by

Deleted: multiple factors including wavelength,

Deleted: (also referred to as terrain height)

Deleted: shape

Deleted: and cloud fraction and altitude

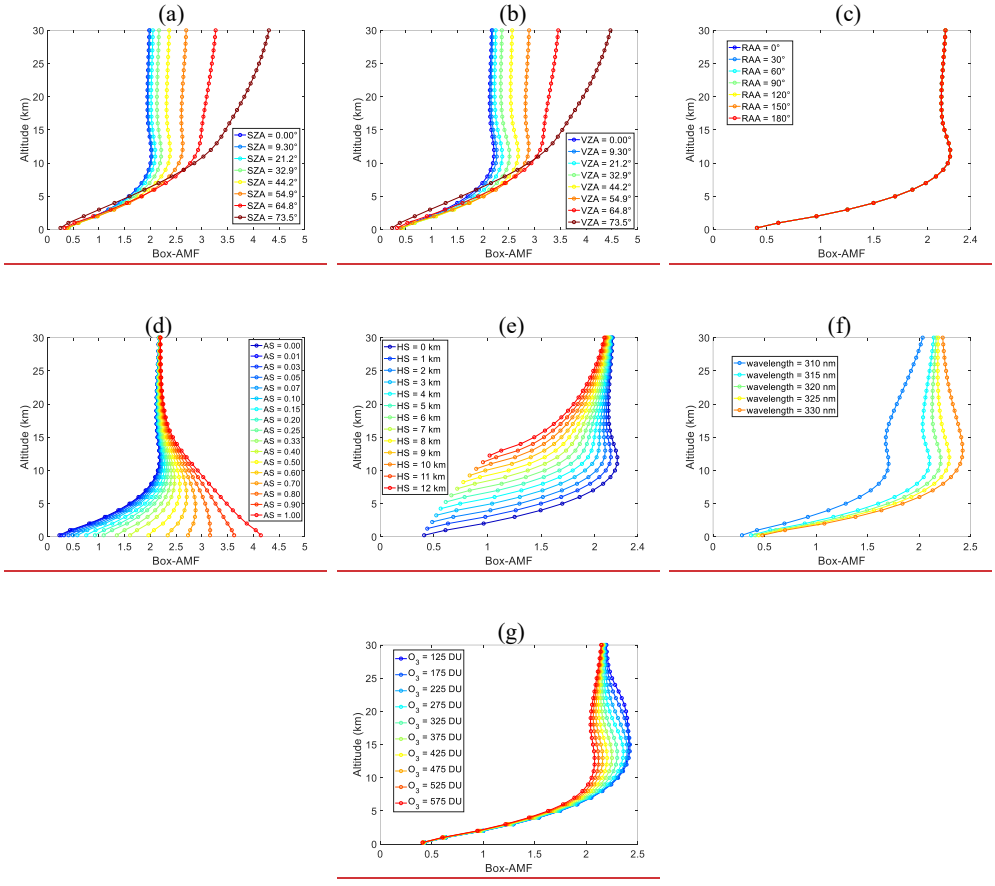

Figure 19: Variation of Box-AMF with SZA, VZA, RAA, AS, HS, wavelength, and O_3 column. The default SCIATRAN settings for Box-AMF calculation are as follows: wavelength=320 nm, clear sky, HS=0 km, O_3=275 DU, AS=0.05, SZA=32.9°, VZA=0°, RAA=0°.

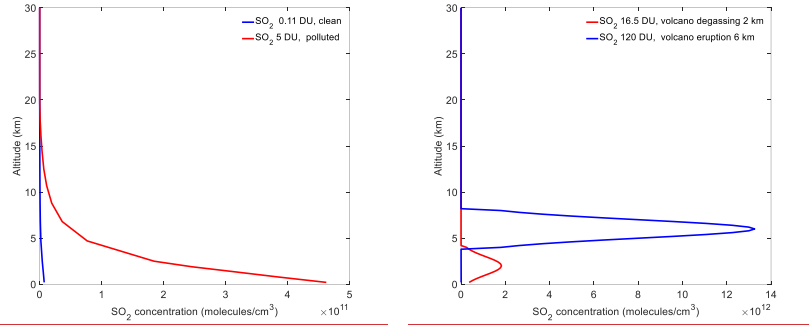

Figure 20: (Left) Assumed SO_2 profiles corresponding to clean conditions, and anthropogenic SO_2 emissions; (Right) Assumed SO_2 profiles corresponding to volcanic degassing with plume heights around 2 km, and volcanic eruption with plume heights around 6 km.

5.2.1 Error source: observation angles (SZA, VZA, RAA)

As shown in Figs. 19a-b, at lower altitudes, Box-AMF is relatively insensitive to changes in SZA and VZA within the range of 0–50°. However, at higher altitudes (e.g., above 5km), the Box-AMF generally increases with increasing SZA and VZA due to the longer atmospheric path length at larger angles, which enhances the contribution of each atmospheric layer to the total AMF. When SZA or VZA exceeds 73.5°, Box-AMFs decrease significantly below altitude 10 km, and larger angles are excluded. As shown in Fig. 19c, the variation of Box-AMF with RAA is negligible. At the time of writing, the measurement errors of OMS SZA and VZA are unavailable, and the proportion of uncertainty propagated to the AMF remains to be determined. In general, satellite measurements of SZA and VZA are considered highly accurate, and their contribution to the overall uncertainty is expected to be negligible.

5.2.2 Error source: surface reflectance (AS)

The surface reflectance has a relatively strong impact on the OMS SO_2 AMF values, especially in anthropogenic emission regions where SO_2 is concentrated near the surface. As shown in Fig. 19d, Box-AMF increases with increasing surface reflectance due to enhanced atmospheric multiple scattering. The difference in surface Box-AMF can reach approximately 1700%.

The OMI surface LER database used for OMS SO_2 AMF calculation has overall uncertainties in the LER of 0.01–0.02, with slightly increasing values at shorter wavelengths (Kleipool et al., 2008). Here, we assume an LER uncertainty of 0.02 and use the SO_2 vertical profiles shown in Fig. 20 to calculate the AMF uncertainty due to AS errors for five scenarios. The results are as follows: (1) AMF uncertainty decreases with increasing AS, indicating that bright surfaces reduce the effect of

Deleted: To analyze the impact of these factors on AMF calculation, we used the SCIATRAN as forward radiative transfer model (Rozanov et al., 2005) to compute Box-AMF under different forward model settings. Box-AMFs corresponding to each set of forward input settings are stored as a function of altitude, representing the atmospheric contribution from each layer. Figure 20 illustrates the variation of SCIATRAN Box-AMF with SZA, VZA, RAA, AS, HS, wavelength, and O_3 column. The forward model settings remain consistent across all cases, except for the variable being analyzed: SZA = 32.9°, VZA = 0°, RAA = 0°, LER AS = 0.05, HS = 0 km, wavelength = 320 nm, O_3 column = 365 DU, clear sky, and with the assumption of surface reflectance as LER.

Deleted: 20

Deleted: Note that w

Deleted: is greater than

Deleted: the

Deleted: has a significant decrease

Deleted: compared to the values at other angles

Deleted: 20

AS perturbations on AMF. (2) Volcanic degassing and polluted conditions are particularly sensitive to AS: at AS = 0.05, uncertainties are ~6.5% and ~5.6%, respectively, while at AS = 0.8, they decrease to ~2.1% and ~2.0%, indicating that AS strongly influences AMF in cases with moderate SO_2 concentrations. (3) High-concentration SO_2 is less sensitive to AS: for volcanic eruption scenarios, AMF uncertainty varies slightly with AS, ranging from 1.1% to 2.1%. These results indicate that accurate AS input is crucial for reliable AMF calculations. In the future, higher spatial resolution surface reflectance products that account for directional effects, such as the TROPOMI DLER model (Tilstra et al., 2024), will be considered for OMS SO_2 AMF calculations.

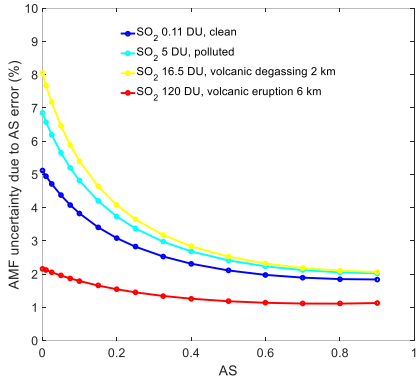

Figure 21: AMF uncertainty due to AS errors for different scenarios.

5.2.3 Error source: terrain height (HS)

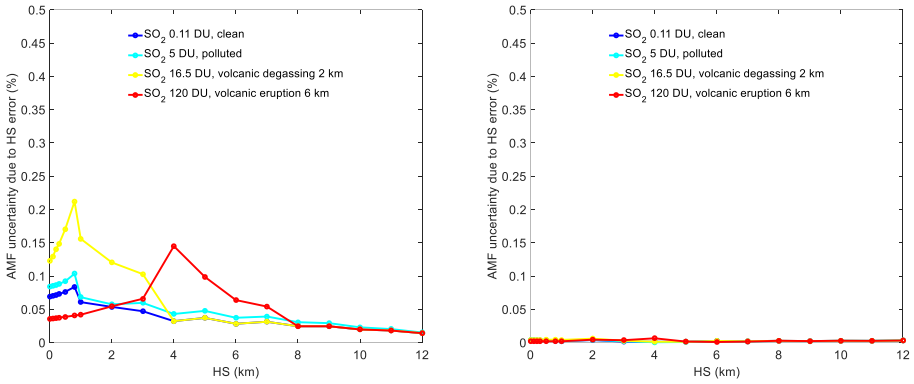

Figure 22: AMF uncertainty due to HS errors for different scenarios. (Left) AS=0.05; (Right) AS=0.8.

The terrain heights used in OMS SO_2 AMF calculations were obtained from the OMS L1 dataset, which derived terrain information from the Copernicus Digital Elevation Model (COP-DEM) with a spatial resolution of 30 m. According to the Copernicus DEM Product Handbook, the product exhibits an absolute vertical accuracy better than 4 m and a horizontal accuracy better than 6 m under standard conditions (Fahrland et al., 2020). Therefore, a terrain height uncertainty of 4 m is assumed to quantify the AMF uncertainty induced by HS errors.

The results (Fig. 22) show that: (1) For AS = 0.05, the AMF uncertainty due to HS errors is relatively small, generally below 0.2%, while for AS = 0.8 it is further reduced to mostly below 0.01%. (2) The AMF uncertainty decreases with increasing surface elevation: low-elevation surfaces (0–1 km) exhibit higher sensitivity, particularly under polluted and volcanic degassing scenarios, whereas at high elevations (>5 km) the uncertainty becomes negligible (<0.02%). (3) The sensitivity to HS varies among different scenarios, which can be attributed to differences in the altitude of SO_2 concentration peaks in each profile.

5.2.4 Error source: SO_2 profile shape

Since the actual vertical distribution of atmospheric SO_2 is often difficult to obtain, a priori profiles from chemical transport models are commonly used in AMF calculations. For regions dominated by anthropogenic emissions, models such as GEOS-Chem and TM5 are widely applied to provide global SO_2 vertical profiles for AMF estimation, and uncertainties in these profiles can propagate into the total AMF.

In this study, SO_2 vertical profiles from GEOS-CF were used for AMF calculations. Keller et al. (2021) reported that GEOS-CF v1.0 systematically overestimates SO_2 concentrations owing to outdated emission inventories, with model biases

Deleted: Box-AMF increases as surface reflectance increases (Fig. 20d) due to higher reflectivity enhancing atmospheric multiple scattering, which increases the photon path length and thereby raises Box-AMF values. When LER surface reflectance changes from 0 to 1, the surface Box-AMF increases from 0.23 to 4.14, an increase of approximately 1700%. However, the increase of surface reflectance also changes the vertical shape of Box-AMF, shifting it from increasing with altitude to decreasing with altitude. Fig. 20e shows that the Box-AMF decreases with increasing terrain height, as higher surface elevation reduces the atmospheric column above the ground, leading to less scattering and decreased sensitivity. (Fahrland et al., 2020)…

Deleted: The variation of Box-AMF with wavelength ranging from 310 nm to 330 nm (Fig. 20f) shows that Box-AMF increases with increasing wavelength. The difference in Box-AMF at different wavelengths varies with altitude. For example, near the surface, when the wavelength increases from 310 nm to 330 nm, the surface Box-AMF increases from 0.28 to 0.48, a rise of 71.13%; At an altitude of 10 km, the Box-AMF increases from 1.69 to 2.36, a rise of 39.57%. Note that for most cases in this study, the wavelength 320 nm, which is approximately at the center of the SO_2 retrieval window (312-326 nm), was chosen to perform the SCIATRAN Box-AMF calculation. The variation of Box-AMF with the O_3 column from 125 DU to 575 DU (Fig. 20g) shows that, compared to other influencing factors, O_3 column has a relatively weak impact on Box-AMF, especially for altitudes below 5 km. The Box-AMF gradually decreases as the O_3 column increases. The differences in Box-AMF under different O_3 column conditions are more noticeable between altitudes of 5 km and 25 km. For example, at an altitude of 15 km, Box-AMF decreases from 2.41 to 2.07 as the O_3 column increases from 125 DU to 575 DU, a decrease of about 14%.…

Deleted:

Deleted: (Keller et al., 2021)

reaching up to a factor of four. However, at the time of writing, detailed information on the layer-resolved uncertainties and temporal biases of GEOS-CF SO_2 vertical profiles is not available. Considering that the GEOS-CF results originate from the GEOS-Chem chemistry module, the uncertainty estimates reported in Lee et al. (2009) were adopted, where the AMF uncertainty due to GEOS-Chem SO_2 profile errors was generally in the range of 10–22% under clear-sky conditions.

5.2.5 Error source: O_3

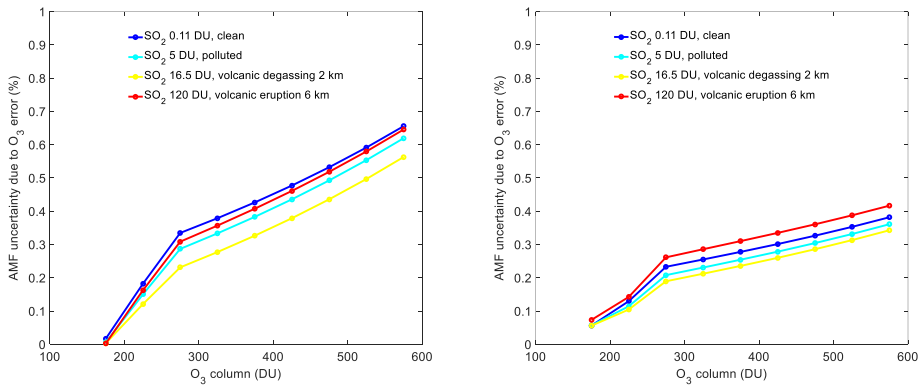

Figure 23: AMF uncertainty due to O_3 errors for different scenarios. (Left) AS=0.05; (Right) AS=0.8.

The variation of Box-AMF with the O_3 column (Fig. 19g) shows that, O_3 column has a relatively weak impact on Box-AMF, especially for altitudes below 5 km. The Box-AMF gradually decreases as the O_3 column increases. The differences in Box-AMF under different O_3 column conditions are more noticeable between altitudes of 5 km and 25 km. In this study, the total O_3 column from OMS was used in the OMS SO_2 AMF calculation, with an estimated uncertainty of less than 5%. Assuming O_3 error of 5%, the estimate of AMF uncertainty due to O_3 errors is generally small (Fig. 23), with values below 0.7% for dark surfaces (AS = 0.05) and below 0.4% for bright surfaces (AS = 0.8). AMF uncertainty increases slightly with increasing O_3 total column, especially for dark surfaces.

5.2.6 Error source: wavelength dependence

The wavelength dependence of AMF is a non-negligible error source of AMF uncertainty. The variation of Box-AMF with wavelength ranging from 310 nm to 330 nm (Fig. 19f) shows that Box-AMF increases with increasing wavelength. In this study, the wavelength 320 nm, which is approximately at the center of the SO_2 retrieval window (312-326 nm), was selected for the AMF calculation. To evaluate the AMF uncertainty due to wavelength dependence, three representative wavelengths within the retrieval window (313 nm, 320 nm, and 325 nm) were selected to quantify the impact of wavelength dependence.

Deleted: (Keller et al., 2021)As seen from the above results, compared to other influencing factors, surface reflectance has a relatively strong impact on Box-AMF, thus affecting the accuracy of AMF calculations, especially in anthropogenic emission regions where SO_2 is concentrated near the surface. The errors of Box-AMF from surface reflectance primarily come from two aspects. One is the errors in the surface reflectance climatology. In many satellite products, for each pixel, a surface reflectance climatology (such as from OMI (Kleipool et al., 2008) or TROPOMI (Tilstra et al., 2024)) is interpolated to obtain the corresponding surface reflectance, which is then used as input to calculate the corresponding Box-AMF. The uncertainties in the surface reflectance climatology and interpolation errors due to the spatial resolution differences between the satellite observations and surface reflectance climatology can degrade the accuracy of the Box-AMF calculations. The sensitivity analysis of AS error on SCIATRAN Box-AMF (Fig. 21), which was conducted by introducing a 1% and 0.01 perturbation in AS values ranging from 0.01 to 0.90, shows that (1) The uncertainties in Box-AMF due to a 1% and 0.01 AS variation show a decreasing trend with increasing altitude, meaning that Box-AMF is more sensitive to AS at lower altitudes. (2) The uncertainties of Box-AMF due to a 1% AS variation increase as the AS increases, while those due to a 0.01 AS variation decrease as the AS increases. When AS is small (e.g., AS = 0.01, 0.03, 0.05), a 1% variation in AS can lead to less than a 0.5% change in Box-AMF near the surface. However, when AS ranges from 0.8 to 0.9, the uncertainties of Box-AMF due to a 1% AS variation can reach up to 1.1%-1.2% near the surface. Another aspect affecting the accuracy of Box-AMF due to surface reflectance is the assumption of surface reflectance as LER during SCIATRAN Box-AMF calculation. Surface reflectivity, which depends on the surface properties and the geometry of incident and reflected light, is not uniformly distributed in all directions (i.e., anisotropy). This anisotropy is typically described by the bidirectional reflectance distribution function (BRDF). However, due to more scattering in the UV, this effect is more relevant at longer wavelengths. Therefore, accurate AS input is crucial for the accuracy of Box-AMF calculation, especially in regions with high surface reflectance.
Neglecting forward model errors, Figure 22 shows the dependence of AMF on SZA, VZA, AS, wavelength, O_3 column, and SO_2 profiles. The AMFs were calculated with SCIATRAN Box-AMFs using six assumed SO_2 profiles. Here six SO_2 profiles were constructed, representing clean conditions, low, medium, and high anthropogenic SO_2 emissions, volcanic degassing with plume heights around 2 km, and volcanic eruptions with plume heights around 6 km. As show ...

Deleted: In future work, we aim to incorporate high-resolution and satellite-synchronized SO_2 vertical profiles to improve the accuracy of AMF.
resolution satellite observations, it is often necessary to build a Box-AMF lookup table (LUT) by using radiative transfer model that considers variables such as SZA, VZA, RAA, AS, HS, wavelength, O_3 column, and cloud cover. The corresponding Box-AMF values for each satellite observation pixel are then obtained through interpolation within the LUT. This approach significantly improves the efficiency of retrieval, avoiding excessive computational time that would result from repeatedly running the radiative transfer model. However, the LUT approach may introduce new errors into the Box-AMF results. First, LUT are typically constructed based on specific atmospheric conditions and forward input parameters, which may not accurately represent real atmospheric conditions. Secondly, the interpolation process within the LUT introduces further uncertainties into the Box-AMF results.

As shown in Table 5, the AMF uncertainty due to wavelength dependence ranges from approximately 5.4% to 6.8% for dark surfaces (AS = 0.05) and decreases to about 3.5%–4.5% for bright surfaces (AS = 0.8). This indicates that AMF is more sensitive to wavelength variations under dark surface conditions, whereas enhanced multiple scattering over bright surfaces reduces the impact of wavelength dependence. Among the four scenarios, polluted conditions and volcanic degassing exhibit larger wavelength-related uncertainties, while clean and volcanic eruption cases show relatively lower sensitivity.

Table 5. AMF uncertainty due to wavelength dependence

	SO_2 profile, 0.11 DU, clean	SO_2 profile, 5 DU, polluted	SO_2 profile, 16.5 DU, volcanic degassing	SO_2 profile, 120 DU, volcanic eruption
AS=0.05	5.43%	6.04%	6.82%	4.48%
AS=0.8	4.17%	4.36%	4.50%	3.54%

5.2.7 Error source: others

In addition to the error sources discussed above, other factors may also contribute to AMF uncertainty. However, their impacts on AMF have not yet been quantitatively assessed in this study. These factors include (1) uncertainties in the radiative transfer model, which are generally considered to be small; (2) interpolation errors. For SO_2 retrievals from high spatial resolution satellite observations, it is often necessary to construct a LUT using a radiative transfer model to improve retrieval efficiency. However, the LUT approach, which requires an interpolation process, may introduce additional uncertainties into the Box-AMF results.

5.2.8 Total AMF uncertainty

Deleted:

Overall, the AMF uncertainty is primarily dominated by uncertainties in surface reflectance, the SO_2 vertical profile shape, and wavelength dependence, while the contributions from ozone and terrain height are relatively small. Assuming that these error sources are independent, the total AMF uncertainty can be expressed as the quadrature sum of the AMF uncertainties due to surface reflectance (AS), terrain height (HS), SO_2 vertical profile shape S(z), O_3 column, and wavelength dependence, as follows:

$$\sigma_{AMF} = \sqrt{(\frac{\partial AMF}{\partial AS}\sigma_{AS})^2 + (\frac{\partial AMF}{\partial HS}\sigma_{HS})^2 + (\frac{\partial AMF}{\partial S(z)}\sigma_{S(z)})^2 + (\frac{\partial AMF}{\partial O_3}\sigma_{O_3})^2 + (\frac{\partial AMF}{\partial \lambda}\sigma_{\lambda})^2}$$

The total AMF uncertainties under five scenarios—clean, boundary layer pollution, boundary layer pollution over snow and ice, volcanic degassing, and volcanic eruption—are estimated to be 12–23%, 13–24%, 11–22%, 14–24%, and >50%, respectively. It should be noted that these values were calculated under clear-sky conditions, without considering the effects of clouds or aerosols.

Deleted:

Deleted:

Table 6. OMS SO_2 AMF uncertainty due to individual error components under different clear-sky scenarios

Error source	Parameter uncertainty	Clean	Boundary layer pollution	Boundary layer pollution over snow and ice	Volcanic degassing	Volcanic eruption
Surface reflectance	0.02	~4%	~6%	~2%	~6%	~2%
Terrain height	4 m	~0.07%	~0.08%	~0.004%	~0.12%	~0.04%
SO_2 vertical profile shape	–	10–22%	10–22%	10–22%	10–22%	Large(>50%)
O_3 column	<5%	~0.3%	~0.3%	~0.2%	~0.2%	~0.3%
Wavelength dependence	–	~5%	~6%	~4%	~7%	~4%
Total uncertainty of OMS SO_2 AMF		12–23%	13–24%	11–22%	14–24%	>50%

5.3 Errors from background offset correction

Background offset correction is essential for the OMS SO_2 column retrievals which have obvious along-track stripes and cross-track asymmetries problems. However, it is hard to get the accurate background offset for SO_2 retrieval of each pixel. In this study, an iterative sliding correction scheme for background offset correction was applied to OMS SO_2 retrievals, with the purpose of forcing SO_2 values over clean or low SO_2 emission regions to zero. This approach helps addressing problems such as along-track stripes and cross-track asymmetry. However, the sliding window strategy assumes that pixels with values smaller than the threshold (2 DU) within the sliding window represent zero SO_2 emissions, which may lead to a loss of SO_2 information contained in the low-emission regions. This not only could limit the applicability of the OMS SO_2 product for monitoring anthropogenic emission sources, but also may lead to many negative retrievals of SO_2 column in clean regions. Furthermore, SO_2 retrievals at certain cross-track positions (assumed to be clean near-zero) may exceed the 2 DU threshold, requiring the threshold to be adjusted upwards to achieve a better effect after background offset correction. Therefore, although the current background offset correction strategy helps mitigate stripes, residual systematic errors may still remain after the correction, which could affect the accuracy of the OMS SO_2 column retrievals.

The quantification of the residual systematic errors is challenging, as it is difficult to fully separate random fitting errors from residual systematic components. Therefore, in this study, the residual systematic errors after the background offset correction were combined with the random fitting errors and treated as an effective SCD uncertainty, which was subsequently used in the total uncertainty estimation of the OMS SO_2 VCD.

5.4 Total uncertainty of OMS SO_2 VCD

In general, assuming that the error sources are independent of each other, the uncertainty of satellite-retrieved SO_2 VCD can be estimated using the following standard error propagation approach (Lee et al., 2009; Theys et al., 2017):

Deleted:

<object>

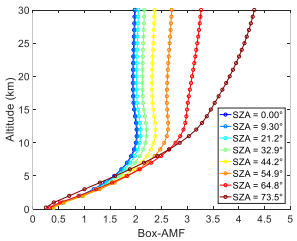

...

Deleted: initial

Deleted: from satellite observations

Deleted: usually

Moved down [2]: However, it is hard to get the accurate background offset for SO_2 retrieval of each pixel. In this study, an

Deleted: systematic overestimation or underestimation problems.

Deleted: initial

Deleted: sliding window

Deleted: background errors

Moved (insertion) [2]

Deleted: it may also affect the accuracy of OMS SO_2 column retrievals.However, it is hard to get the accurate background offset for SO_2 retrieval of each pixel.…

$$\sigma_{SO_2} = \sqrt{\left(\frac{\sigma_{SCD}}{AMF}\right)^2 + \left(\frac{\sigma_{SCD}^{back}}{AMF}\right)^2 + \left(\frac{(SCD - SCD^{back}) \cdot \sigma_{AMF}}{AMF^2}\right)^2} \quad \text{(Eq. 4)}$$

where σ_{SCD} is the random error from DOAS SO_2 SCD spectral fitting including instrument-related noise, σ_{SCD}^{back} is the residual systematic error after background offset correction, and σ_{AMF} is the AMF uncertainty which includes two components: one is related to the atmospheric scattering weight and the other one is associated with the SO_2 profile shape.

In the standard error propagation method, σ_{SCD} is commonly approximated by the SFE. However, for the OMS SO_2 retrieval, the SFE is strongly affected by instrument-related systematic errors, as shown in Fig. 18. As a result, the SFE includes not only random fitting errors but also systematic components, and thus does not represent the random SCD uncertainty. If directly used as σ_{SCD} in the error propagation, it would lead to an overestimation of the total uncertainty of the OMS SO_2 VCD.

Therefore, the SFE was not adopted as σ_{SCD} in this study. Instead, the standard deviation of the corrected SCD over clean oceanic regions, approximately 0.2 DU in equatorial regions and about 0.4 DU at high latitudes, was used as an effective SCD uncertainty. This value reflects the combined effect of random fitting error and residual systematic errors after background offset correction and was propagated into the total uncertainty estimation. Accordingly, the total uncertainty of the OMS SO_2 VCD can be expressed as:

$$\sigma_{SO_2} = \sqrt{\left(\frac{\sigma_{SCD,res}}{AMF}\right)^2 + \left(\frac{SCD_{corr} \cdot \sigma_{AMF}}{AMF^2}\right)^2} \quad \text{(Eq. 5)}$$

where $\sigma_{SCD,res}$ is the effective SCD uncertainty, and SCD_{corr} is the background-corrected SO_2 SCD.

The estimated total uncertainties of OMS SO_2 VCDs under four scenarios —clean, boundary layer pollution, volcanic degassing, and volcanic eruption—are summarized in Table 7. The results show that under clean conditions, the total uncertainty is dominated by measurement noise and fitting errors, ranging from 0.16–0.17 DU at low latitudes and 0.32–0.33 DU at high latitudes. The corresponding relative errors are ~150% at low latitudes and ~295% at high latitudes, reflecting the challenge of retrieving low SO_2 column. For boundary layer pollution scenarios, the enhanced SO_2 signal reduces the relative errors to 14–25%, while the total uncertainty increases to 0.68–1.21 DU at low latitudes and 0.75–1.26 DU at high latitudes. For volcanic degassing, the relative errors range from 14–24%, with total uncertainties ranging from 2.32 to 3.97 DU. Under the volcanic eruption scenario, the total uncertainty and relative error are approximately 60 DU and 50%, respectively. It should be noted that these estimates still involve large uncertainties due to the large errors in radiance measurement and SO_2 vertical profile provided by GEOS-CF, particularly under volcanic eruption conditions. In addition, the uncertainties associated with clouds and aerosols were not included in the present error analysis, suggesting that the estimated uncertainties may be conservative.

Table 7. Total uncertainty of OMS SO_2 VCDs under different clear-sky scenarios

Scenario	Total uncertainty (DU)	Relative error (%)
Clean	Low latitude: 0.16–0.17 DU High latitude: 0.32–0.33 DU	Low latitude: ~150% High latitude: ~295%
Boundary layer pollution	Low latitude: 0.68–1.21 DU High latitude: 0.75–1.26 DU	Low latitude: 14–25% High latitude: 15–25%
Volcanic degassing	2.32–3.97 DU	14–24%
Volcanic eruption	~60 DU	~50%

6 Conclusions and future work

This study presents the first SO_2 retrieval results from the Chinese FY-3F/OMS instrument, which was launched in August 2023. The results were derived using TOA reflected radiance data from FY-3F/OMS with a DOAS approach. To improve the retrieval accuracy, specific processing schemes were developed based on the characteristics of the OMS instrument and the performance of its L1 data. These schemes, including solar spectrum selection, spectral soft calibration, and background offset correction, effectively reduce along-track stripes and across-track asymmetry in the OMS SO_2 retrievals.

To evaluate the accuracy of OMS SO_2 retrievals, comparisons with TROPOMI DOAS and TROPOMI COBRA SO_2 products were conducted over clean oceanic regions, volcanic eruptions, and anthropogenic emission regions. The comparison results indicate that OMS retrievals show reasonable agreement with TROPOMI products, have good stability in clean oceanic regions and can be used to monitor SO_2 emissions from volcanic eruptions and anthropogenic sources. In selected clean oceanic regions, the SO_2 values of both OMS and TROPOMI follow approximately a normal distribution centered around 0, with most values concentrated between -2 DU and 2 DU. For the Sundhnúkur and Nyamuragira volcanic eruptions, FY-3F/OMS SO_2 retrievals successfully capture the spatial distribution and high-concentration plumes of volcanic SO_2, similar to the TROPOMI DOAS and TROPOMI COBRA 7 km SO_2 results. However, OMS tends to underestimate SO_2 at high columns (>50 DU) due to saturation in the 312–326 nm fitting window. In anthropogenic emission regions, OMS and TROPOMI SO_2 products show generally good consistency in detecting anthropogenic SO_2 emissions, with correlation coefficients ranging from about 0.6–0.9 over the Persian Gulf and 0.80–0.85 over Norilsk. The differences between OMS and TROPOMI SO_2 results may be related to differences in local overpass times, spatial resolution, observation angles, and the L1 and L2 processing algorithms (e.g., differences in L1 radiometric and spectral calibration methods, SO_2 retrieval fitting windows, AMF strategies).

In summary, the agreement between the OMS and TROPOMI measurements is within expectations, taking into account the differences in satellite overpass times and the uncertainties associated with AMF. With its high spectral and spatial resolution, morning overpass time, daily global coverage, and reliable SO_2 retrieval results, OMS will provide effective data

Deleted: utilized TOA reflected radiance data from the Chinese FY3F/OMS-N instrument, launched in August 2023 to retrieve global SO_2 columns with a DOAS approach. Based on the characteristics of the OMS instrument and the performance of its L1 data, specific schemes including solar spectrum selection, spectral soft calibration, and background offset correction were developed to effectively reduce along-track stripes and across-track asymmetry in the initial OMS SO_2 retrievals.

Deleted: The OMS SO_2 retrievals were compared

Deleted: in

Deleted: under

Deleted: condition

Deleted: in

Deleted: regions

Deleted: FY3F/OMS

Deleted: Over the Sundhnúkur volcano, OMS and TROPOMI DOAS show a high correlation of ~0.87, and OMS and TROPOMI COBRA reach ~0.76, indicating good overall agreement. …

Deleted: 5

Deleted: 6

Deleted: up to

Deleted: 9

Deleted: 1

Deleted: 93

Deleted:

Deleted: Among these, the AMF used in the SO_2 column retrieval is a major contributor to the differences between OMS and TROPOMI SO_2 results. For example, in the case of the Sundhnúkur volcano, the lack of accurate information on the vertical SO_2 profile can lead to discrepancies of more than a factor of two when comparing the OMS and TROPOMI SO_2 results. Random noise and uncertainties from background correction are relevant for low SO_2 scenarios, such as over the Persian Gulf, and lead to scatter in the order of several DU. However, the results for Norilsk demonstrate that under relatively constant emission conditions, good agreement can be achieved with a simple AMF when the satellite overpass times are well matched. …

Deleted: assumptions

support for monitoring the continuous SO_2 changes from global volcanic eruptions and anthropogenic activities, helping to fill the spatial and temporal gaps in the existing global satellite network.

The current OMS SO_2 retrievals still have several shortcomings that need to be addressed in the future. More work will be needed to incorporate accurate and satellite-synchronized SO_2 vertical profiles to improve the accuracy of AMF. In addition, higher spatial resolution surface reflectance products that account for directional effects, as well as the impacts of clouds and aerosols on the AMF, should be considered in the OMS SO_2 AMF calculation. Another issue that needs to be addressed in the future is the simultaneous retrieval of volcanic eruption heights, which would help improve the accuracy of SO_2 retrievals in volcanic regions. Moreover, the 312–326 nm retrieval fitting window used in the OMS SO_2 product exhibits nonlinear variation in the case of very large SO_2 concentrations, leading to an underestimation of SO_2 columns. In the future, SO_2 retrievals from longer UV wavelength fitting windows varying with SO_2 columns will be incorporated into the OMS SO_2 retrieval to mitigate the saturation issue in the case of large volcanic eruptions. Our preliminary strategy for such retrievals is as follows. First, a global SO_2 column retrieval is performed using the 312–326 nm window. Pixels exceeding a threshold (e.g., >50 DU) are flagged as potentially saturated. For these flagged pixels, additional retrievals are conducted using the 325–335 nm and 360–390 nm windows. If the new retrievals are within a reasonable range and exceed the 312–326 nm results, the maximum value from the 325–335 nm or 360–390 nm windows replaces the original retrieval; otherwise, the 312–326 nm retrieval is retained.

Furthermore, although in this study the comparison between OMS SO_2 retrievals and TROPOMI SO_2 products was conducted to demonstrate the capability of OMS SO_2 retrievals, synchronous and high-quality ground-based or airborne measurements remain crucial for validating the accuracy of OMS SO_2 retrievals. In the future, ground-based and airborne experiments need to be conducted to provide accurate ground-based or airborne data for the validation of OMS SO_2 retrievals.

Deleted: Due to the lack of a prior SO_2 and temperature profiles, a simplified approach that uses two constant AMF values for typical conditions was applied for the OMS SO_2 conversion from SCD to VCD in this study. …

Deleted: Additionally,

Deleted: operational

Deleted: products

Author contribution

HY: Drafting, data processing, and plotting; AR: Revision, research methodology and content suggestions, and English polishing; XZ: Suggestions on revision and research direction; AS: Discussion and suggestions on the Ring effect; TV & YL & CY: Discussion and suggestions on AMF calculation; QW: Discussion on the data quality of OMS L1 data; LZ & WW: Discussion and suggestions on the revision of the Error analysis section.

Deleted: Huanhuan Yan

Deleted: ndreas Richter

Deleted: ingying Zhang

Deleted: nja Schönhardt

Deleted: homas

Deleted: isarius

Deleted: & LC

Deleted: .

Data Availability

The SO_2 data produced in this study is available from the authors on request. FY-3F/OMS-N L1 data can be downloaded from the website http://data.nsmc.org.cn/DataPortal/en/home/index.html. TROPOMI DOAS SO_2 data is available via the

Deleted: FY3F/OMS

Copernicus Data Space Ecosystem (https://browser.dataspace.copernicus.eu/). TROPOMI COBRA SO_2 data is available via the PAL system (https://data-portal.s5p-pal.com/products/so2cbr.html).

Acknowledgements

This study has been supported by the National Key Research and Development Program of China under Grant 2022YFB3904801. The authors wish to thank the many scientists and engineers from FY-3F/OMS L1 team, TROPOMI team, and the Institute of Environmental Physics at the University of Bremen. The authors also acknowledge the use of ChatGPT for improving the English of the manuscript.

References

Bauduin, S., Clarisse, L., Clerbaux, C., Hurtmans, D., and Coheur, P. F.: IASI observations of sulfur dioxide (SO_2) in the boundary layer of Norilsk, J Geophys Res-Atmos, 119, 4253-4263, 2014.

Boersma, K., Eskes, H., and Brinksma, E.: Error analysis for tropospheric NO_2 retrieval from space, J Geophys Res-Atmos, 109, 2004.

Bogumil, K., Orphal, J., Homann, T., Voigt, S., Spietz, P., Fleischmann, O. C., Vogel, A., Hartmann, M., Kromminga, H., Bovensmann, H., Frerick, J., and Burrows, J. P.: Measurements of molecular absorption spectra with the SCIAMACHY pre-flight model: instrument characterization and reference data for atmospheric remote-sensing in the 230–2380 nm region, Journal of Photochemistry and Photobiology A: Chemistry, 157, 167-184, 2003.

Burrows, J. P., Weber, M., Buchwitz, M., Rozanov, V., Ladstätter-Weißenmayer, A., Richter, A., DeBeek, R., Hoogen, R., Bramstedt, K., and Eichmann, K.-U.: The global ozone monitoring experiment (GOME): Mission concept and first scientific results, J Atmos Sci, 56, 151-175, 1999.

Carn, S. A., Krueger, A. J., Krotkov, N. A., Yang, K., and Evans, K.: Tracking volcanic sulfur dioxide clouds for aviation hazard mitigation, Nat Hazards, 51, 325-343, DOI 10.1007/s11069-008-9228-4, 2009.

Carn, S. A., Krueger, A. J., Krotkov, N. A., Yang, K., and Levelt, P. F.: Sulfur dioxide emissions from Peruvian copper smelters detected by the Ozone Monitoring Instrument, Geophys Res Lett, 34, 1093-1101, 10.1029/2006gl029020, 2007.

Carn, S., Strow, L. d., de Souza-Machado, S., Edmonds, Y., and Hannon, S.: Quantifying tropospheric volcanic emissions with AIRS: The 2002 eruption of Mt. Etna (Italy), Geophys Res Lett, 32, 2005.

Chance, K. V. and Spurr, R. J.: Ring effect studies: Rayleigh scattering, including molecular parameters for rotational Raman scattering, and the Fraunhofer spectrum, Appl Optics, 36, 5224-5230, 1997.

Chen, L., Han, D., Tao, J., and Su, L.: Overview of tropospheric NO_2 vertical column density retrieval from space measurement, Journal of Remote Sensing, 13, 343-360, 2009.

Chen, L., Shang, H., Fan, M., Tao, J., Husi, L., Zhang, Y., Wang, H., Cheng, L., Zhang, X., and Wei, L.: Mission overview of

Deleted: FY3F/OMS

Deleted: 10.1016/s1010-6030(03)00062-5,

Deleted:

Deleted: Burrows, J. P., Weber, M., Buchwitz, M., Rozanov, V., Ladstatter-Weissenmayer, A., Richter, A., DeBeek, R., Hoogen, R., Bramstedt, K., Eichmann, K. U., and Eisinger, M.: The global ozone monitoring experiment (GOME): Mission concept and first scientific results, J Atmos Sci, 56, 151-175, Doi 10.1175/1520-0469(1999)056<0151:Tgomeg>2.0.Co;2, 1999.

Deleted: Carn, S. A., Strow, L. L., de Souza-Machado, S., Edmonds, Y., and Hannon, S.: Quantifying tropospheric volcanic emissions with AIRS: The 2002 eruption of Mt. Etna (Italy), Geophys Res Lett, 32, Artn L02301

the GF-5 satellite for atmospheric parameter monitoring, National Remote Sensing Bulletin, 25, 1917-1931, 2021.

Coddington, O. M., Richard, E. C., Harber, D., Pilewskie, P., Woods, T. N., Chance, K., Liu, X., and Sun, K.: The TSIS-1 hybrid solar reference spectrum, Geophys Res Lett, 48, e2020GL091709, 2021.

Cofano, A., Cigna, F., Santamaria Amato, L., Siciliani de Cumis, M., and Tapete, D.: Exploiting Sentinel-5P TROPOMI and ground sensor data for the detection of volcanic SO_2 plumes and activity in 2018–2021 at Stromboli, Italy, Sensors-Basel, 21, 6991, 2021.

Corradino, C., Jouve, P., La Spina, A., and Del Negro, C.: Monitoring Earth's atmosphere with Sentinel-5 TROPOMI and Artificial Intelligence: Quantifying volcanic SO_2 emissions, Remote Sens Environ, 315, 114463, 2024.

Cullis, C. F. and Hirschler, M. M.: Atmospheric Sulfur - Natural and Man-Made Sources, Atmos Environ, 14, 1263-1278, Doi 10.1016/0004-6981(80)90228-0, 1980.

Eisinger, M. and Burrows, J. P.: Tropospheric sulfur dioxide observed by the ERS-2 GOME instrument, Geophys Res Lett, 25, 4177-4180, Doi 10.1029/1998gl900128, 1998.

Fahrland, E., Jacob, P., Schrader, H., and Kahabka, H.: Copernicus digital elevation model product handbook, Airbus Defence and Space—Intelligence: Potsdam, Germany, 2024-2006, 2020.

Finlayson-Pitts, B. J. and Pitts Jr, J. N.: Chemistry of the upper and lower atmosphere: theory, experiments, and applications, Elsevier1999.

Fioletov, V., McLinden, C. A., Griffin, D., Theys, N., Loyola, D. G., Hedelt, P., Krotkov, N. A., and Li, C.: Anthropogenic and volcanic point source SO_2 emissions derived from TROPOMI on board Sentinel-5 Precursor: first results, Atmos Chem Phys, 20, 5591-5607, 2020.

Fioletov, V., McLinden, C., Krotkov, N., Yang, K., Loyola, D., Valks, P., Theys, N., Van Roozendael, M., Nowlan, C., and Chance, K.: Application of OMI, SCIAMACHY, and GOME-2 satellite SO_2 retrievals for detection of large emission sources, J Geophys Res-Atmos, 118, 11,399-311,418, 2013.

Fish, D. and Jones, R.: Rotational Raman scattering and the ring effect in zenith-sky spectra, Geophys Res Lett, 22, 811-814, 1995.

Flynn, L. E., Seftor, C. J., Larsen, J. C., and Xu, P.: The Ozone Mapping and Profiler Suite, 2006.

Global Volcanism Program, 2024. Report on Nyamuragira (DR Congo) (Sennert, S, ed.). Weekly Volcanic Activity Report, 6 November-12 November 2024. Smithsonian Institution and US Geological Survey.

Global Volcanism Program, 2024. Report on Reykjanes (Iceland) (Sennert, S, ed.). Weekly Volcanic Activity Report, 21 August-27 August 2024. Smithsonian Institution and US Geological Survey.

Gottwald, M. and Bovensmann, H.: SCIAMACHY-Exploring the changing Earth's Atmosphere, Springer Science & Business Media2010.

Heue, K. P., Brenninkmeijer, C. A. M., Wagner, T., Mies, K., Dix, B., Frieß, U., Martinsson, B. G., Slemr, F., and van Velthoven, P. F. J.: Observations of the 2008 Kasatochi volcanic SO_2 plume by CARIBIC aircraft DOAS and the GOME-2 satellite, Atmos Chem Phys, 10, 4699-4713, 10.5194/acp-10-4699-2010, 2010.

Deleted: Grainger, J. and Ring, J.: Anomalous Fraunhofer line profiles, Nature, 193, 762-762, 1962.

Keller, C. A., Knowland, K. E., Duncan, B. N., Liu, J., Anderson, D. C., Das, S., Lucchesi, R. A., Lundgren, E. W., Nicely, J. M., and Nielsen, E.: Description of the NASA GEOS composition forecast modeling system GEOS-CF v1.0, Journal of Advances in Modeling Earth Systems, 13, e2020MS002413, 2021.

Khokhar, M. F., Frankenberg, C., Van Roozendael, M., Beirle, S., Kühl, S., Richter, A., Platt, U., and Wagner, T.: Satellite observations of atmospheric SO_2 from volcanic eruptions during the time-period of 1996–2002, Adv Space Res, 36, 879-887, 10.1016/j.asr.2005.04.114, 2005.

Kleipool, Q., Dobber, M., de Haan, J., and Levelt, P.: Earth surface reflectance climatology from 3 years of OMI data, J Geophys Res-Atmos, 113, 2008.

Krotkov, N. A., Carn, S. A., Krueger, A. J., Bhartia, P. K., and Yang, K.: Band residual difference algorithm for retrieval of SO_2 from the aura Ozone Monitoring Instrument (OMI), IEEE Trans. Geosci. Remote Sensing, 44, 1259-1266, Doi 10.1109/Tgrs.2005.861932, 2006.

Krotkov, N. A., McLinden, C. A., Li, C., Lamsal, L. N., Celarier, E. A., Marchenko, S. V., Swartz, W. H., Bucsela, E. J., Joiner, J., and Duncan, B. N.: Aura OMI observations of regional SO_2 and NO_2 pollution changes from 2005 to 2015, Atmos Chem Phys, 16, 4605-4629, 2016.

Krotkov, N. A., McClure, B., Dickerson, R. R., Carn, S. A., Li, C., Bhartia, P. K., Yang, K., Krueger, A. J., Li, Z. Q., Levelt, P. F., Chen, H. B., Wang, P. C., and Lu, D. R.: Validation of SO_2 retrievals from the Ozone Monitoring Instrument over NE China, J Geophys Res-Atmos, 113, 259-269, 2008.

Krueger, A. J.: Sighting of El Chichón Sulfur Dioxide Clouds with the Nimbus 7 Total Ozone Mapping Spectrometer, Science, 220, 1377-1379, DOI 10.1126/science.220.4604.1377, 1983.

Kuttippurath, J., Patel, V. K., Pathak, M., and Singh, A.: Improvements in SO_2 pollution in India: role of technology and environmental regulations, Environ Sci Pollut R, 29, 78637-78649, 2022.

Lee, C., Martin, R. V., van Donkelaar, A., O'Byrne, G., Krotkov, N., Richter, A., Huey, L. G., and Holloway, J. S.: Retrieval of vertical columns of sulfur dioxide from SCIAMACHY and OMI: Air mass factor algorithm development, validation, and error analysis, J Geophys Res, 114, 10.1029/2009jd012123, 2009.

Levelt, P. F., Van den Oord, G. H. J., Dobber, M. R., Malkki, A., Visser, H., de Vries, J., Stammes, P., Lundell, J. O. V., and Saari, H.: The Ozone Monitoring Instrument, IEEE Trans. Geosci. Remote Sensing, 44, 1093-1101, Doi 10.1109/Tgrs.2006.872333, 2006.

Li, C., Joiner, J., Krotkov, N. A., and Bhartia, P. K.: A fast and sensitive new satellite SO_2 retrieval algorithm based on principal component analysis: Application to the ozone monitoring instrument, Geophys Res Lett, 40, 6314-6318, 2013.

Lorente, A., Folkert Boersma, K., Yu, H., Dörner, S., Hilboll, A., Richter, A., Liu, M., Lamsal, L. N., Barkley, M., and De Smedt, I.: Structural uncertainty in air mass factor calculation for NO_2 and HCHO satellite retrievals, Atmos Meas Tech, 10, 759-782, 2017.

Mardani, M., Nowrouzi, M., and Abyar, H.: Assessing the environmental impact of offshore flares in the Persian Gulf: A comprehensive analysis of SO_2 emissions, Advances in Environmental Technology, 11, 63-74, 2025.

Deleted: Artn D16s40
Doi 10.1029/2007jd008818,

Mccormick, M. P., Thomason, L. W., and Trepte, C. R.: Atmospheric effects of the Mt. Pinatubo eruption, Nature, 373, 399-404, Doi 10.1038/373399a0, 1995.

Miller, T., P. and Casadevall, T., J.: Volcanic ash hazards to aviation, in: Encyclopedia of Volcanoes, edited by: Sigurdsson, H., Academic Press, San Diego, 915-930, 2000.

Munro, R., Eisinger, M., Anderson, C., Callies, J., Corpaccioli, E., Lang, R., Lefebvre, A., Livschitz, Y., and Albiñana, A. P.: GOME-2 on MetOp, Proc. of The 2006 EUMETSAT Meteorological Satellite Conference, Helsinki, Finland, 12—16 June, 12-16,

Newhall, C. G. and Self, S.: The volcanic explosivity index (VEI) an estimate of explosive magnitude for historical volcanism, Journal of Geophysical Research: Oceans, 87, 1231-1238, 1982.

Nowlan, C., Liu, X., Chance, K., Cai, Z., Kurosu, T., Lee, C., and Martin, R.: Retrievals of sulfur dioxide from the Global Ozone Monitoring Experiment 2 (GOME-2) using an optimal estimation approach: Algorithm and initial validation, J Geophys Res-Atmos, 116, 2011.

Palmer, P. I., Jacob, D. J., Chance, K., Martin, R. V., Spurr, R. J., Kurosu, T. P., Bey, I., Yantosca, R., Fiore, A., and Li, Q.: Air mass factor formulation for spectroscopic measurements from satellites: Application to formaldehyde retrievals from the Global Ozone Monitoring Experiment, J Geophys Res-Atmos, 106, 14539-14550, 2001.

Platt, U. and Stutz, J.: Differential Optical Absorption Spectroscopy: Principles and Applications, Physics of Earth and Space Environments, Springer, Verlag Berlin Heidelberg, 593 pp., 10.1007/978-3-540-75776-4 2008.

Richter, A.: Algorithm Theoretical Basis Document for the GOME-2 Rapid Volcanic SO_2 product, SAVAA project.[Available at https://www.iup.uni-bremen.de/doas/so2_alerts/gome2_so2_atbd_091005.pdf], 2009.

Richter, A., Wittrock, F., and Burrows, J. P.: SO_2 measurements with SCIAMACHY, Proc. Atmospheric Science Conference, Frascati, Italy, 8 -12 May, 8-12,

Rozanov, A., Rozanov, V., Buchwitz, M., Kokhanovsky, A., and Burrows, J.: SCIATRAN 2.0–A new radiative transfer model for geophysical applications in the 175–2400 nm spectral region, Adv Space Res, 36, 1015-1019, 2005.

Seinfeld, J. H. and Pandis, S. N.: Atmospheric chemistry and physics: from air pollution to climate change, John Wiley & Sons2016.

Sioris, C. E. and Evans, W. F.: Filling in of Fraunhofer and gas-absorption lines in sky spectra as caused by rotational Raman scattering, Appl Optics, 38, 2706-2713, 1999.

Theys, N., Campion, R., Clarisse, L., Brenot, H., Van Gent, J., Dils, B., Corradini, S., Merucci, L., Coheur, P.-F., and Van Roozendael, M.: Volcanic SO_2 fluxes derived from satellite data: a survey using OMI, GOME-2, IASI and MODIS, Atmos Chem Phys, 13, 5945-5968, 2013.

Theys, N., De Smedt, I., Yu, H., Danckaert, T., van Gent, J., Hörmann, C., Wagner, T., Hedelt, P., Bauer, H., and Romahn, F.: Sulfur dioxide retrievals from TROPOMI onboard Sentinel-5 Precursor: algorithm theoretical basis, Atmos Meas Tech, 10, 119-153, 2017.

Theys, N., Hedelt, P., De Smedt, I., Lerot, C., Yu, H., Vlietinck, J., Pedergnana, M., Arellano, S., Galle, B., and Fernandez,

Deleted: Sinnhuber, B.-M., Sheode, N., Sinnhuber, M., Chipperfield, M., and Feng, W.: The contribution of anthropogenic bromine emissions to past stratospheric ozone trends: a modelling study, Atmos Chem Phys, 9, 2863-2871, 2009.

D.: Global monitoring of volcanic SO_2 degassing with unprecedented resolution from TROPOMI onboard Sentinel-5 Precursor, Sci Rep-Uk, 9, 2643, 2019.

Theys, N., Fioletov, V., Li, C., De Smedt, I., Lerot, C., McLinden, C., Krotkov, N., Griffin, D., Clarisse, L., Hedelt, P., Loyola, D., Wagner, T., Kumar, V., Innes, A., Ribas, R., Hendrick, F., Vlietinck, J., Brenot, H., and Van Roozendael, M.: A sulfur dioxide Covariance-Based Retrieval Algorithm (COBRA): application to TROPOMI reveals new emission sources, Atmos. Chem. Phys., 21, 16727-16744, 10.5194/acp-21-16727-2021, 2021.

Tilstra, L. G., de Graaf, M., Trees, V. J., Litvinov, P., Dubovik, O., and Stammes, P.: A directional surface reflectance climatology determined from TROPOMI observations, Atmos Meas Tech, 17, 2235-2256, 2024.

Twomey, S.: The influence of pollution on the shortwave albedo of clouds, Journal of Atmospheric Sciences, 34, 1149-1152, 1977.

van Geffen, J. H. and van Oss, R. F.: Wavelength calibration of spectra measured by the Global Ozone Monitoring Experiment by use of a high-resolution reference spectrum, Appl Optics, 42, 2739-2753, 2003.

Vandaele, A. C., Hermans, C., and Fally, S.: Fourier transform measurements of SO_2 absorption cross sections: II. Temperature dependence in the 29 000-44 000 cm(-1) (227-345 nm) region, J Quant Spectrosc Ra, 110, 2115-2126, DOI 10.1016/j.jqsrt.2009.05.006, 2009.

Veefkind, J., Aben, I., McMullan, K., Förster, H., De Vries, J., Otter, G., Claas, J., Eskes, H., De Haan, J., and Kleipool, Q.: TROPOMI on the ESA Sentinel-5 Precursor: A GMES mission for global observations of the atmospheric composition for climate, air quality and ozone layer applications, Remote Sens Environ, 120, 70-83, 2012.

Voors, R., De Vries, J., Bhatti, I. S., Lobb, D., Wood, T., Nick, V. D. V., Aben, I., and Veefkind, P.: TROPOMI, the Sentinel 5 precursor instrument for air quality and climate observations: status of the current design, Society of Photo-optical Instrumentation Engineers,

Vountas, M., Rozanov, V., and Burrows, J.: Ring effect: Impact of rotational Raman scattering on radiative transfer in Earth's atmosphere, Journal of Quantitative Spectroscopy and Radiative Transfer, 60, 943-961, 1998.

Wagner, T., Burrows, J., Deutschmann, T., Dix, B., Von Friedeburg, C., Frieß, U., Hendrick, F., Heue, K.-P., Irie, H., Iwabuchi, H., Kanaya, Y., Keller, J., McLinden, C. A., Oetjen, H., Palazzi, E., Petritoli, A., Platt, U., Postylyakov, O., Pukite, J., Richter, A., van Roozendael, M., Rozanov, A., Rozanov, V., Sinreich, R., Sanghavi, S., and Wittrock, F.: Comparison of box-air-mass-factors and radiances for Multiple-Axis Differential Optical Absorption Spectroscopy (MAX-DOAS) geometries calculated from different UV/visible radiative transfer models, Atmos Chem Phys, 7, 1809-1833, 2007.

Wang, C., Wang, T., Wang, P., and Wang, W.: Assessment of the performance of TROPOMI NO_2 and SO_2 data products in the North China Plain: comparison, correction and application, Remote Sens-Basel, 14, 214, 2022.

Wang, Q., Wang, Y., Xu, N., Mao, J., Sun, L., Shi, E., Hu, X., Chen, L., Yang, Z., and Si, F.: Preflight Spectral Calibration of the Ozone Monitoring Suite-Nadir on FengYun 3F Satellite, Remote Sens-Basel, 16, 1538, 2024.

Xu, J., Wang, Y., Chen, L., Efremenko, D., Rao, L., Tana, G., Liu, S., Wang, Q., Mao, J., and Wang, Y.: First total ozone column observations from the Ozone Monitoring Suite-Nadir (OMS-N) onboard China's FengYun-3F satellite, Science

Deleted: Twomey, S.: The Influence of Pollution on the Shortwave Albedo of Clouds, J Atmos Sci, 34, 1149-1152, 10.1175/1520-0469(1977)034<1149:TIOPOT>2.0.CO;2, 1977.…

China Earth Sciences, 68, 3665-3683, 2025.

Yan, H., Wang, W., and Chen, L.: Temperature effects on the retrieval of SO_2 from ultraviolet satellite observations, Remote Sensing of the Atmosphere, Clouds, and Precipitation V, 379-386,

Yan, H., Wang, H., Wang, W., and Zhang, X.: Volcanic SO_2 retrieved from GF-5 Environmental trace gas Monitoring Instrument, National Remote Sensing Bulletin, 25, 2326-2338, 10.11834/jrs.20210303, 2021.

Yan, H., Li, X., Wang, W., Zhang, X., Chen, L., Han, D., Yu, C., and Gao, L.: Comparison of SO_2 column retrievals from BRD and DOAS algorithms, Science China Earth Sciences, 60, 1694-1706, 2017.

Yang, K., Dickerson, R. R., Carn, S. A., Ge, C., and Wang, J.: First observations of SO_2 from the satellite Suomi NPP OMPS: Widespread air pollution events over China, Geophys Res Lett, 40, 4957-4962, 2013.

Yang, K., Krotkov, N. A., Krueger, A. J., Carn, S. A., Bhartia, P. K., and Levelt, P. F.: Retrieval of large volcanic SO_2 columns from the Aura Ozone Monitoring Instrument: Comparison and limitations, J Geophys Res, 112, D24S43, doi: 10.1029/2007JD008825, 2007.

Yang, K., Krotkov, N. A., Krueger, A. J., Carn, S. A., Bhartia, P. K., and Levelt, P. F.: Improving retrieval of volcanic sulfur dioxide from backscattered UV satellite observations, Geophys Res Lett, 36, 2009.

Yang, K., Liu, X., Bhartia, P. K., Krotkov, N. A., Carn, S. A., Hughes, E. J., Krueger, A. J., Spurr, R. J., and Trahan, S. G.: Direct retrieval of sulfur dioxide amount and altitude from spaceborne hyperspectral UV measurements: Theory and application, J Geophys Res-Atmos, 115, 2010.

Zhao, M., Si, F., Wang, Y., Zhou, H., Wang, S., Jiang, Y., and Liu, W.: First Year On-Orbit Calibration of the Chinese Environmental Trace Gas Monitoring Instrument Onboard GaoFen-5, IEEE Trans. Geosci. Remote Sensing, 58, 8531-8540, 2020.

Deleted:

Deleted: Fahrland, E., Jacob, P., Schrader, H., and Kahabka, H.: Copernicus digital elevation model product handbook, Airbus Defence and Space—Intelligence: Potsdam, Germany, 2024-2006, 2020.